NASA
CR
3373
c.1

LOAN COPY RE
AFWL TECHNIC
KIRTLAND AFB,

0062298

TECH LIBRARY KAFB, NM

NASA Contractor Report 3373

Jet Array Impingement With Crossflow - Correlation of Streamwise Resolved Flow and Heat Transfer Distributions

L. W. Florschuetz, D. E. Metzger,
and C. R. Truman

GRANT NSG-3075
JANUARY 1981

NASA

TECH LIBRARY KAFB, NM
0062298

NASA Contractor Report 3373

Jet Array Impingement With Crossflow - Correlation of Streamwise Resolved Flow and Heat Transfer Distributions

L. W. Florschuetz, D. E. Metzger,
and C. R. Truman
Arizona State University
Tempe, Arizona

Prepared for
Lewis Research Center
under Grant NSG-3075

NASA
National Aeronautics
and Space Administration

**Scientific and Technical
Information Branch**

1981

CONTENTS

NOMENCLATURE

A	= coefficient of Reynolds number in power function fit or correlation equations
A_o^*	= ratio of jet hole area to opposing heat transfer surface area (open area ratio)
b	= thickness of jet plate
B	= coefficient in crossflow function of correlation equation
β	= flow distribution parameter introduced following Eq. (3.7), $C_D \sqrt{2}(\pi/4)/[y_n/d)/(z/d)]$
C	= constant appearing in correlation equation
C_D	= jet plate discharge coefficient
d	= jet hole diameter
G_c	= crossflow mass velocity based on channel cross-sectional area
G_j	= jet mass velocity based on jet hole area
G_j^*	= superficial jet mass velocity based on jet plate or equivalent opposing heat transfer surface area
h	= convective heat transfer coefficient resolved in streamwise direction, averaged across span
i	= spanwise hole row number
k	= thermal conductivity of fluid
L	= streamwise length of heat transfer surface
m	= Reynolds number exponent in power function fit or correlation equation
M	= flow distribution parameter introduced at Eq. (3.4), $\sqrt{2} A_o^* C_D/z$
μ	= dynamic viscosity
n	= exponent in crossflow function of correlation equation
n_x, n_y, n_z	= constants appearing in correlation equation

Nu = Nusselt number resolved in streamwise direction, averaged across span, hd/k

Nu_1 = value of Nu at first upstream spanwise row of holes where $G_c/G_j = 0$

N_c = number of spanwise rows of jet holes

N_s = number of jet holes across span of heat transfer surface

N_s' = number of jet holes across span of channel

P = channel pressure

P_e = channel exhaust pressure

P_o = plenum pressure

Pr = Prandtl number

Re_j = jet Reynolds number, $G_j d/\mu$

ρ = fluid density

T_o = plenum air temperature

T_r = recovery or adiabatic wall temperature at impingement surface

T_s = impingement surface temperature

x = streamwise location along heat transfer surface measured from upstream end of channel

x_n = streamwise jet hole spacing

y_n = spanwise jet hole spacing

z = channel height (jet plate-to-impingement surface spacing)

Subscripts

I or S = where distinction is required I refers to inline hole pattern, S refers to staggered

Superscripts

$(\overline{\ })$ = overbar refers to mean value

SUMMARY

Correlations for heat transfer coefficients for jets of air issuing from arrays of circular orifices and impinging on a surface parallel to the jet orifice plate are presented. The air, following impingement, is constrained to exit in a single direction along the channel formed by the jet orifice plate and the heat transfer (impingement) surface. Outlet flow from upstream jets imposes a crossflow on those downstream. Impingement surface heat transfer coefficients resolved to one streamwise jet orifice spacing, averaged across the channel span, are correlated with the associated individual spanwise orifice row jet and crossflow velocities, and with the geometric parameters. The correlations are based on an extensive set of heat transfer data previously obtained and documented in an earlier NASA Contractor Report. The configurations tested model those of interest in current and contemplated designs for cooling of the midchord region of gas turbine airfoils. Both inline and staggered patterns of jet orifice arrays were included in the test program.

The streamwise distributions of jet and crossflow velocities utilized in developing the correlations are based on a theoretical model which was verified by extensive flow distribution measurements obtained as a part of the same test program which resulted in the heat transfer data. The model is a discrete application of a continuous one-dimensional momentum-flux analysis which results in a simple closed form expression for the flow distribution. Both the model and the flow distribution measurements are presented, discussed and compared in this report. Discharge coefficients for each jet orifice plate included in the test program were also measured.

Streamwise hole spacings ranged from 5 to 15 jet hole diameters for inline patterns and 5 to 10 diameters for staggered patterns, spanwise spacings were 4 to 8 diameters, and channel heights (jet plate-to-impingement surface spacings) were 1 to 3 diameters. Hole pattern aspect ratios (ratio of streamwise-to-spanwise hole spacing) ranged from 0.625 to 3.75. The number of spanwise rows of jet holes was fixed at 10 for all configurations. Mean jet Reynolds numbers ranged from about 5×10^3 to 5×10^4. Overall, individual spanwise row jet Reynolds numbers were as low as 2.5×10^3 and as high as 7×10^4. The ratio of the channel crossflow velocity to the jet velocity ranged from zero (at the first upstream row) to as high as 0.8 downstream.

Streamwise jet flow distributions ranged from highly nonuniform for a spanwise hole spacing of four hole diameters and a channel height of one diameter to essentially uniform for a spanwise spacing of eight diameters and a channel height of three diameters. The distributions were essentially independent of streamwise hole spacing and hole pattern.

Separate correlations were required for the inline and staggered hole patterns, since the staggered patterns resulted in smaller heat transfer coefficients than their inline counterparts as hole spacings were decreased and channel height was increased. The correlations are, however, of the same form. Overall, 95% of the total of 2080 data points on which the correlations are based fall within 11% of the corresponding values predicted by the correlations.

1. INTRODUCTION

Impingement with high velocity gas jets has become an established method of convectively cooling or heating surfaces in a wide variety of process and thermal control applications. Examples include cooling of gas turbine airfoils and electronic equipment, drying of paper and textile or other thin layers of films, annealing of metals, and glass tempering operations. The most commonly used jet openings are slots and circular holes. For applications requiring highly localized heating or cooling a single circular jet may suffice. For long, but very narrow areas a single row of circular jets or a single slot jet may be appropriate. The single row or slot may also be adequate, in some cases, for treating sheets of material which can be moved continuously past the row or slot. However, where all portions of a surface of larger expanse must be continuously heated or cooled, multiple slot jets or two-dimensional arrays of jet orifices are required.

For gas turbine engines a significant application utilizing a two-dimensional array of jets is the cooling of the midchord region of gas turbine airfoils. One such arrangement is illustrated in Fig. 1.1. Impingement air from the midchord array flows rearward along the channel formed between the inlet plenum and the airfoil envelope, discharging at the trailing edge. Flow from the upstream jets in the array imposes a crossflow on those located downstream. In this arrangement air discharged from the jet row provided for cooling of the leading edge is then used to provide localized film cooling, and does not interact with the midchord array jets. However, in alternate arrangements, leading edge cooling air is permitted to flow rearward inside the airfoil envelope where it becomes an initial crossflow influence on the midchord array.

In addition to the increased heat rates attainable relative to nonimpinging flows, the jet array provides the designer with potential for a high degree of control of the distribution of surface heat transfer characteristics. By varying the flow and geometric parameters, including the number, size, and spacing of the jet orifices as well as the orifice plate-to-cooled surface height, the potential exists for adjustment of the

heat transfer coefficients to achieve a specified distribution in surface temperature or heat flux.

For the cooled gas turbine airfoil, it should ultimately be possible to account for the variation in the external hot gas heat transfer coefficients and arrive at an optimum internal impingement array that minimizes the required amount of coolant flow. Such an optimum array will, in general, be irregular, but modern chemical machining methods make this quite feasible. Such optimization will require a detailed knowledge of the effect of array geometry on the internal impingement heat transfer characteristics including the effect of the crossflow.

It appears that knowledge of the effects of array configuration on heat transfer characteristics has been inadequate for achievement of optimal designs, even when consideration is restricted to uniformly spaced arrays. Gauntner, et al [1], recently reported results of measurements on an actual gas turbine vane with midchord cooling provided by a uniformly spaced two-dimensional jet array. These results illuminated the inadequacy of existing correlations for predicting heat transfer performance of such arrays. In particular, the study revealed that questions remained unanswered concerning the important crossflow influence on downstream heat transfer as a function of array geometry.

The present investigation was initiated with the primary objective of determining heat transfer behavior for a range of uniformly spaced array configurations which model those of interest in current and contemplated gas turbine airfoil cooling applications. The first phase of the test program was designed to model impingement cooling of the midchord region according to the scheme indicated in Fig. 1.1. The laboratory configuration used to model this midchord cooling scheme is illustrated schematically in Fig. 1.2. The test facility was designed, however, to also permit subsequent testing in the presence of an initial crossflow introduced upstream of the array.

The original test program included the measurement of both mean and chordwise (or streamwise) resolved heat transfer coefficients for uniform rectangular (inline) arrays of jets as a function of flow rate and geometric parameters, with the objective of developing a correlation which would be of direct use to the designer. Subsequently, the program was expanded to include

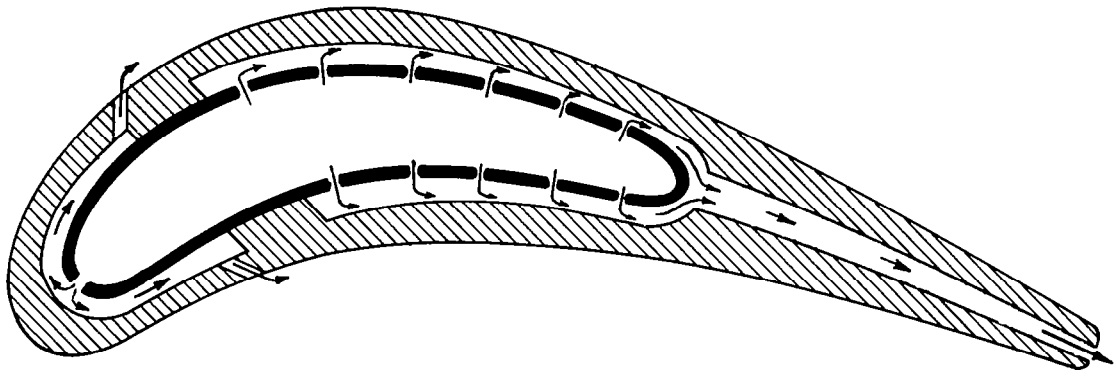

Fig. 1.1 Example of cooled gas turbine airfoil with midchord cooling by jet array impingement scheme.

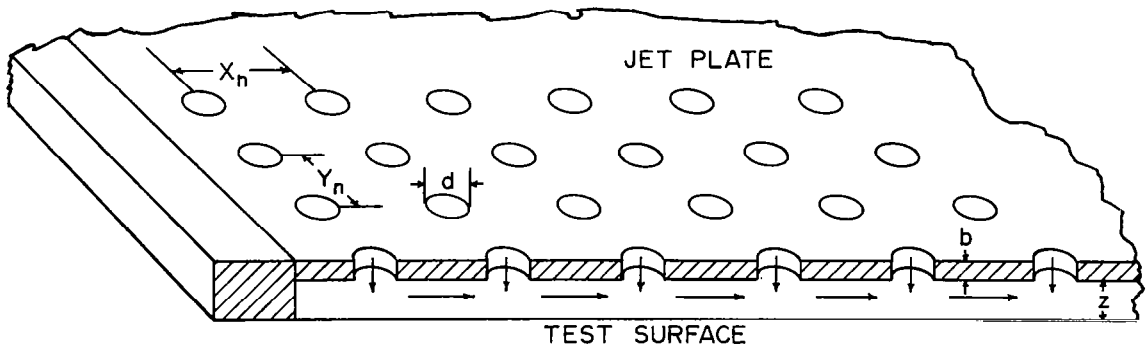

Fig. 1.2 Basic test model geometry and nomenclature.

staggered jet hole array patterns as well as determination of chordwise jet flow distributions. The overall objective, then, became that of developing, for design application, correlations of chordwise resolved heat transfer coefficients as a function of: (1) jet and crossflow rates associated with the individual spanwise jet rows, and (2) geometric parameters.

A previous report [2] provided a detailed description of the basic heat transfer test rig, documented the extensive chordwise resolved and mean heat transfer results obtained for both the inline and staggered patterns as a function of overall or mean flow rate, and presented and discussed the observed trends and characteristics of the data.

Subsequently, the use of a simple one-dimensional momentum flux model was found to quite accurately predict the row-by-row streamwise flow distribution. In this report both development of the model and experimental determination of the flow distributions are presented and the results compared. These flow distributions then provide the means by which the spanwise averaged, streamwise resolved Nusselt numbers are examined as a function of the individually associated spanwise row jet Reynolds numbers and crossflow-to-jet velocity ratios. Correlations are then presented for both inline and staggered hole patterns for Nusselt numbers resolved to one streamwise hole spacing. Specifically, these Nusselt numbers are correlated in terms of the individual spanwise row jet Reynolds number (Re_j) and crossflow-to-jet velocity ratio (G_c/G_j); and in terms of three geometric parameters: the streamwise hole spacing, the spanwise hole spacing, and the channel height each normalized by hole diameter (x_n/d, y_n/d, and z/d). The overall ranges of these variables are for Re_j, 2.5×10^3 to 7×10^4; for G_c/G_j, zero to 0.8; for x_n/d, 5 to 15 for inline hole patterns and 5 to 10 for staggered patterns; for y_n/d, 4 to 8; and for z/d, 1 to 3. The aspect ratios, x_n/y_n, for the jet arrays ranged from 0.625 to 3.75.

The number of spanwise rows of holes for each array was fixed at ten. The range of mean jet Reynolds numbers ($\overline{Re}_j$) was 5×10^3 to 5×10^4. The thickness of the jet orifice plate was maintained equal to the hole diameter. The thermal boundary condition at the impingement surface was isothermal. Tests were run for geometrically similar configurations of different sizes in order to examine scaling effects. Overall, hole diameters ranged from

0.0635 cm (0.025 in.) to 0.762 cm (0.3 in) and heat transfer surface lengths from 6.35 cm (2.5 in) to 38.1 cm (15.0 in.). The larger size configurations permitted better spatial resolution of heat transfer coefficients. The highest streamwise resolution obtained was one-third of the streamwise hole spacing. This resolution permitted observation of pronounced periodic streamwise variations in the heat transfer coefficients [2,3]. Heat transfer coefficients resolved to one or two streamwise hole spacings did not reflect the periodic variations, but showed the streamwise trends smoothed across the periodic variations [2,4].

Prior heat transfer studies for two-dimensional arrays of circular impinging jets with flow constrained to exit in a single direction parallel to jet hole rows were reported by Friedman and Mueller [5], Huang [6], Kercher and Tabakoff [7], and Chance [8]. These studies provided either mean heat transfer results or were limited to spatial resolutions greater than or equal to one streamwise hole spacing. Studies which included some high resolution measurements, but in which the flow was not constrained to exit in a single direction were carried out by Gardon and Cobonpue [9] and Hollworth and Berry [10]. A recent review of impinging jet flow heat and mass transfer was provided by Martin [11]. Metzger and Korstad [12] measured mean heat transfer coefficients for a single row of circular impinging jets normal to a cross-flowing air stream. High resolution studies of a single circular impinging jet in the presence of a crossflow were carried out by Bouchez and Goldstein [13] and by Sparrow, Goldstein and Rouf [14].

2. EXPERIMENTAL FACILITY

A detailed description of the test facility may be found in [2]. However, for the convenience of the reader in interpreting subsequent material in this report, a shortened but essentially complete description is included here along with a complete summary of the significant characteristics of the jet array geometries tested.

The test facility consists overall of a compressed air supply, an air flow metering section, and interchangeable plenum/jet plate assemblies which produce arrays of jets impinging on an instrumented heat transfer test surface. Chordwise (i.e., streamwise) and spanwise cross-sectional views of the assembly of the major components are shown in Fig. 2.1 for one plenum size. A single test plate unit consisting of a segmented copper test plate with individual segment heaters, the necessary thermal insulation, and the test plate support structure, is utilized for all tests. The segmented design provides for control of the streamwise thermal boundary condition at the heat transfer test surface, as well as for determination of spatially resolved heat transfer coefficients in the streamwise direction. The jet plate under test, positioned by the jet plate holder, is bolted to the lower flange of the plenum, which in turn, is bolted to the test plate unit. The jet plate lower surface is positioned relative to the heat transfer surface via interchangeable spacers to permit covering the desired range of z/d.

Laboratory compressed air is piped to the plenum and passed through the plenum packing to provide a uniform flow upstream of the jet plate. After passing through the jet plate the air exhausts to atmospheric pressure by flowing along the channel formed by the jet plate, the test surface, and the spacer.

There are four interchangeable plenums, each of a different streamwise length. Thus, the channel length varies depending on the size of the particular plenum/jet plate assembly being utilized. The thermally active length of the test plate consists, for a given test, of those test plate segments which are immediately opposite the jet plate. The maximum active chordwise length is 38.1 cm (15 in.) (30 segments by 1.27 cm (0.5 in.) per segment), with an additional segment at the downstream end to serve as a guard

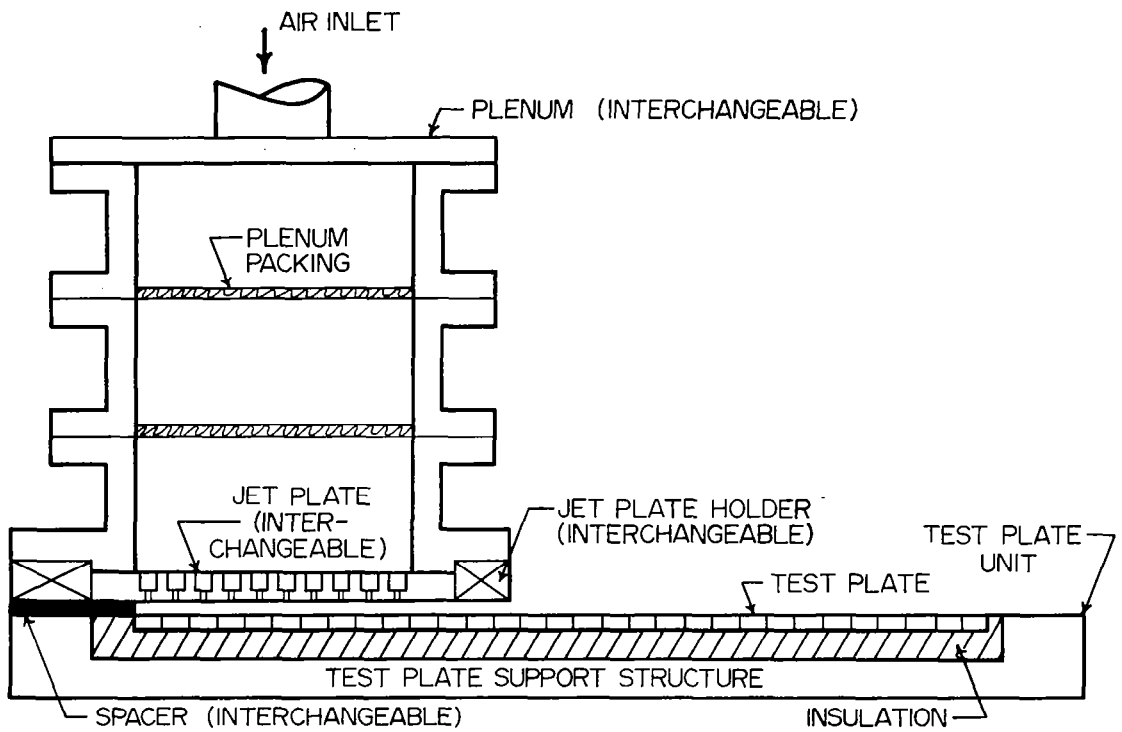

CHORDWISE VIEW

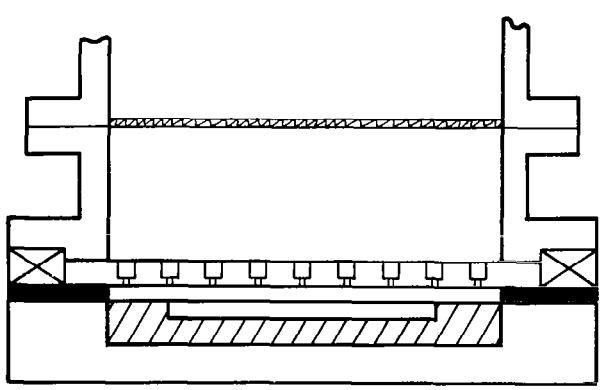

SPANWISE VIEW

Fig. 2.1 Test unit assembly.

element. For tests in which only a fraction of the test plate was thermally active the segment immediately downstream of the active portion served as a guard element.

The jet plate thickness, b, at each hole location is equal to the jet hole diameter. This was achieved by appropriately counterboring plates of larger overall thickness (Fig. 2.1). This design feature was dictated primarily by the need to insure accurate channel heights during test runs, a particularly critical requirement for the narrowest channel height (.0635 cm). The counterbore was three jet hole diameters, except for the narrowest hole spacing where two jet hole diameters was used. In one test with z/d = 1, a 2d counterbore plate was used with the counterbored holes subsequently bored out to 3d, and the test repeated. The results were identical to within experimental uncertainty.

The significant dimensions and geometric characteristics unique to the interchangeable plenums and matching jet plates for which data was obtained are summarized in Table 2.1. The smallest jet hole diameter is near prototype size for the gas turbine application, while the larger sizes provided for improved streamwise resolution of heat transfer coefficients. The relation between the spanwise jet hole rows and the test plate segments is indicated in Fig. 2.2 for jet plates corresponding to each plenum size. Emphasis in this report is placed on results from the B, C, and D sizes since, for these, heat transfer coefficients can be resolved to at least one streamwise hole spacing. Note that the number of spanwise rows of holes was fixed at 10 for all jet plates. The first row (counting from upstream) was always displaced $x_n/2$ from the upstream end of the channel (Fig. 2.2). Each jet plate with a staggered hole pattern was identical to its inline counterpart, except that alternating spanwise rows were offset by one-half the spanwise hole spacing (Fig. 2.3).

Each individual configuration tested can be uniquely identified by specifying a size designation (A, B, C, or D), a set of geometric parameters ($x_n/d, y_n/d, z/d$), and a hole pattern (I or S). For brevity, specific configurations will be referred to by designations such as B(5,8,2)I; or when it is unnecessary to indicate in this way a specific size, hole pattern, and/or geometric paramter value, obvious notations such as B(5,8)I, B(5,8), or simply (5,8) will be used.

Table 2.1 Geometric Characteristics of Configurations Tested

Plenum Size	L cm (inches)	d & b cm (inches)	x_n/d	y_n/d	z/d	① Hole Patterns	② N_s	N'_s	$\bar{C}_D$ I	$\bar{C}_D$ S	# of Active Segments	Maximum Chordwise Resolution	Channel Length cm (inches)
A	6.35(2.5)	0.0635(0.025)	10	6	1,2,3,6	I,S	32	48	--	0.80	5	$2x_n$	10.8(4.25)
				8	1,2,3	I	24	36	0.83	--			
B	12.7(5.0)	0.254(0.100)	5	4	1,2,3	I,S	12	18	0.85	0.85	10	x_n	17.1(6.75)
				8	1,2,3,6	I,S	6	9	0.80	0.79			
		0.127(0.050)	10	4	1,2,3	I,S	24	36	0.76	0.73			
				8	1,2,3	I,S	12	18	0.76	0.74			
C	25.4(10.0)	0.508(0.200)	5	4	1,2,3	I	6	9	0.81	--	20	$\frac{1}{2} x_n$	29.8(11.75)
				6	1,2,3	I	4	6	0.77	--			
				8	1,2,3	I,S	3	4	0.78	0.78			
		0.254(0.100)	10	4	1,2,3	I,S	12	18	0.82	0.83			
				6	1,2,3	I	8	12	0.79	--			
				8	1,2,3	I,S	6	9	0.79	0.80			
D	38.1(15.0)	0.762(0.300)	5	4	1,2,3	I	4	6	0.81	0.79	30	$\frac{1}{3} x_n$	41.3(16.25)
					1,3	S							
		0.381(0.150)	10	4	1,2,3	I	8	12	0.80	--			
				8	1,2,3	I	4	6	0.78	--			
		0.254(0.100)	15	4	1,2,3	I	12	18	0.83	--			
				6	1,2,3	I	8	12	0.80	--			
				8	1,2,3	I	6	9	0.79	--			

Notes: ① I denotes inline hole pattern, S denotes staggered.
② The number of holes across the test plate span, N_s, varies depending on hole spacing; the number along the chord, $N_c = \ell/x_n$, was fixed at 10 for all tests reported herein.

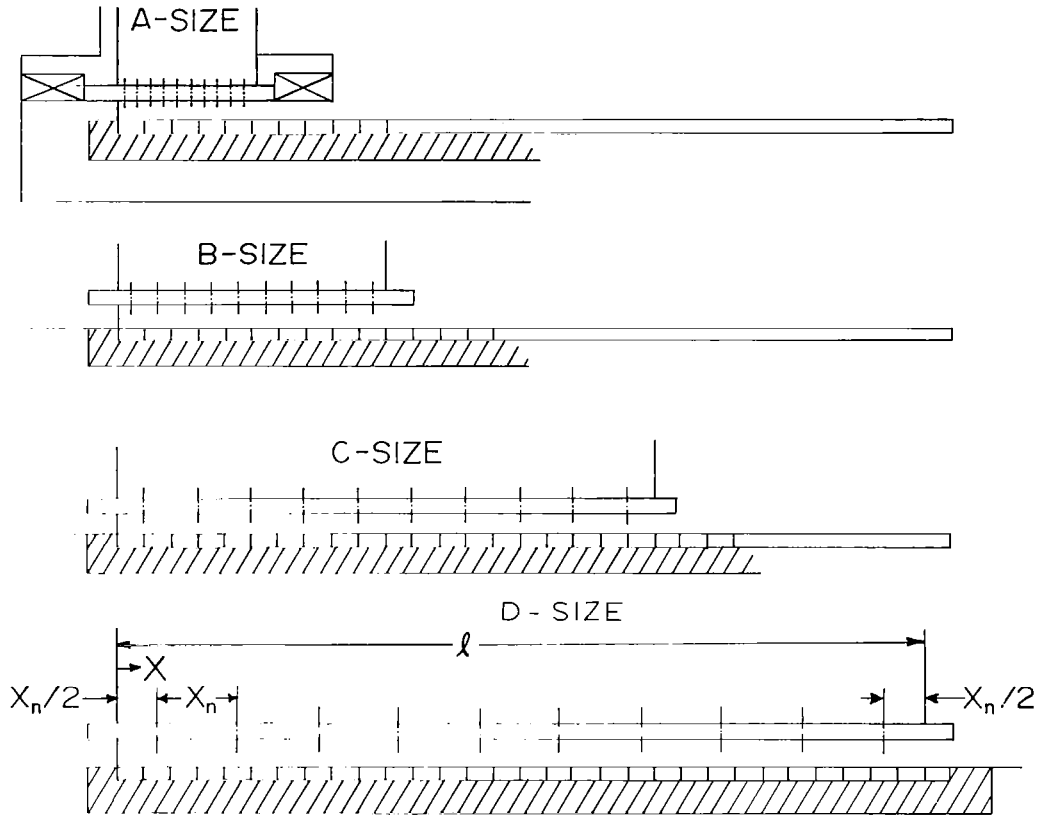

Fig. 2.2 Location of spanwise jet hole rows relative to test plate segments.

Attention is called to the fact that a number of the configurations of different sizes listed in Table 2.1 are geometrically similar. Considering sizes B, C, and D the maximum length scale factor is 3; including A-size, the maximum factor is 6.

The discharge coefficients summarized in Table 2.1 were employed in determination of the row-by-row streamwise flow distributions, as discussed in the next section.

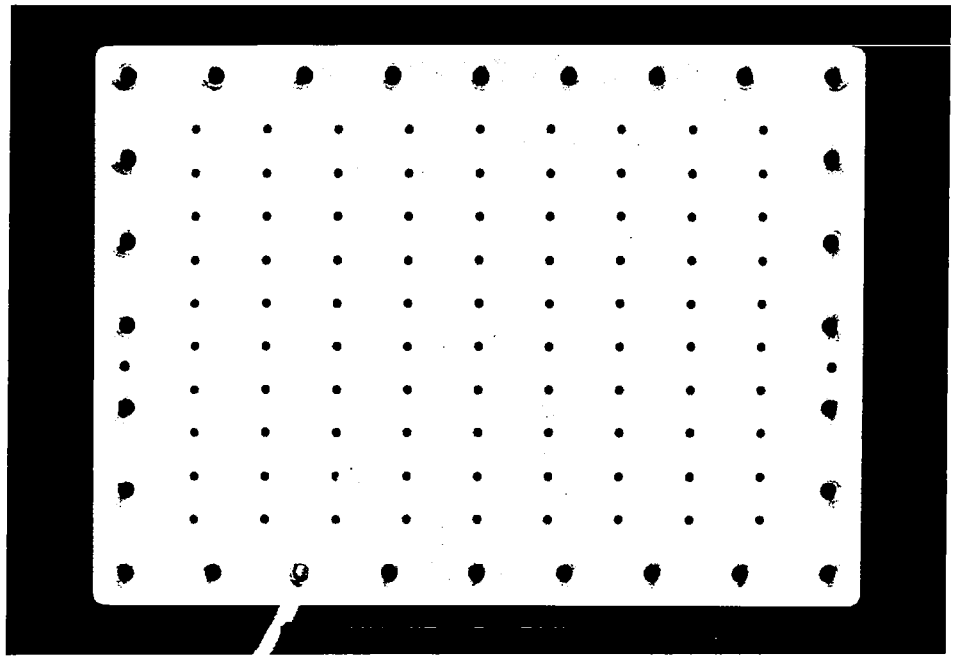

Inline Pattern

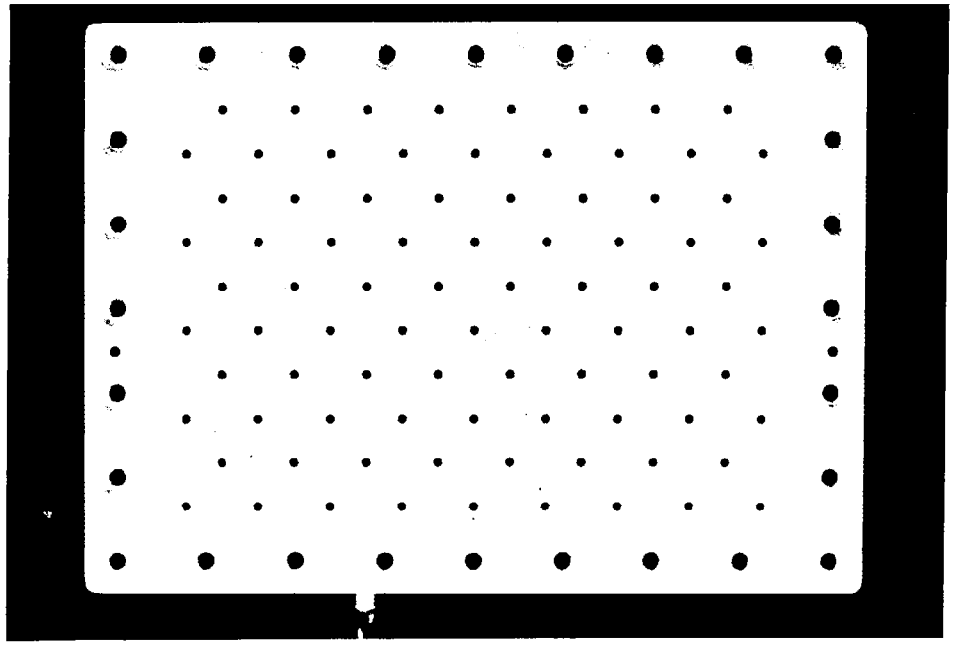

Staggered Pattern

Flow
Direction
(Chordwise)

Fig. 2.3 Corresponding inline and staggered jet array hole patterns illustrated for configuration B(5,8).

3. FLOW DISTRIBUTION

The determination of the distribution of the jet flow among the individual spanwise rows was an essential step prior to attempting correlation of the streamwise resolved heat transfer coefficients with the individual row jet and crossflow rates. The flow distributions were determined from measured streamwise channel pressure profiles and jet plate discharge coefficients. A one-dimensional incompressible momentum flux model was also developed which predicted the experimentally determined flow distributions quite satisfactorily.

3.1 Pressure Traverses and Discharge Coefficients

Streamwise channel pressure traverses were accomplished with static pressure probes inserted from the downstream end of the channel. The probes were stainless steel tubes of 0.0635 to 0.124 cm (0.025 to 0.049 in.) outside diameter closed at the upstream end, with a single orifice of 0.0254 cm (0.010 in.) diameter located 0.318 cm (1/8 in.) from the end. For a given run the tube was positioned along one lower corner of the channel and pressed against the channel side wall and bottom by slightly bowing the tube. This positioning provided support of the tube, thus preventing vibration and possible whipping in the presence of a strong channel flow. The larger diameter tubes were used with larger channel heights which were also associated with longer channel lengths, thus requiring a stiffer probe.

For a given traverse the orifice was positioned either facing upward toward the jet plate, downward toward the channel lower surface, or toward the channel sidewall. For each jet plate configuration, two or three traverses were usually made, each utilizing a different one of these orifice positions. Manometer readings of the channel pressure were normally made at each spanwise jet row location, midway between jet rows, and in some instances at the farthest possible upstream position, $x = 0.318$ cm (1/8 in.). Readings were also normally taken at several positions in the channel downstream of the last (tenth) row of jet holes, the channel exit section.

The pressure profile results for the B(10,8,3)I configuration are plotted in Fig. 3.1 in terms of the ratio of the channel pressure, P, to the plenum pressure, P_o. The locations of the spanwise jet rows are indicated by the vertical arrows along the abscissa. Comparison of results for the three orifice positions as well as the smoothness of the points in traversing from locations immediately opposite jet rows to midway between rows indicates that dynamic pressure effects were not significant.

For the larger channel heights, z/d = 3 as in Fig. 3.1, the channel pressure was fairly uniform, resulting, as will be seen, in a fairly uniform flow distribution. In these cases most of the pressure drop from plenum to exit occurs across the holes rather than along the channel. The pressure

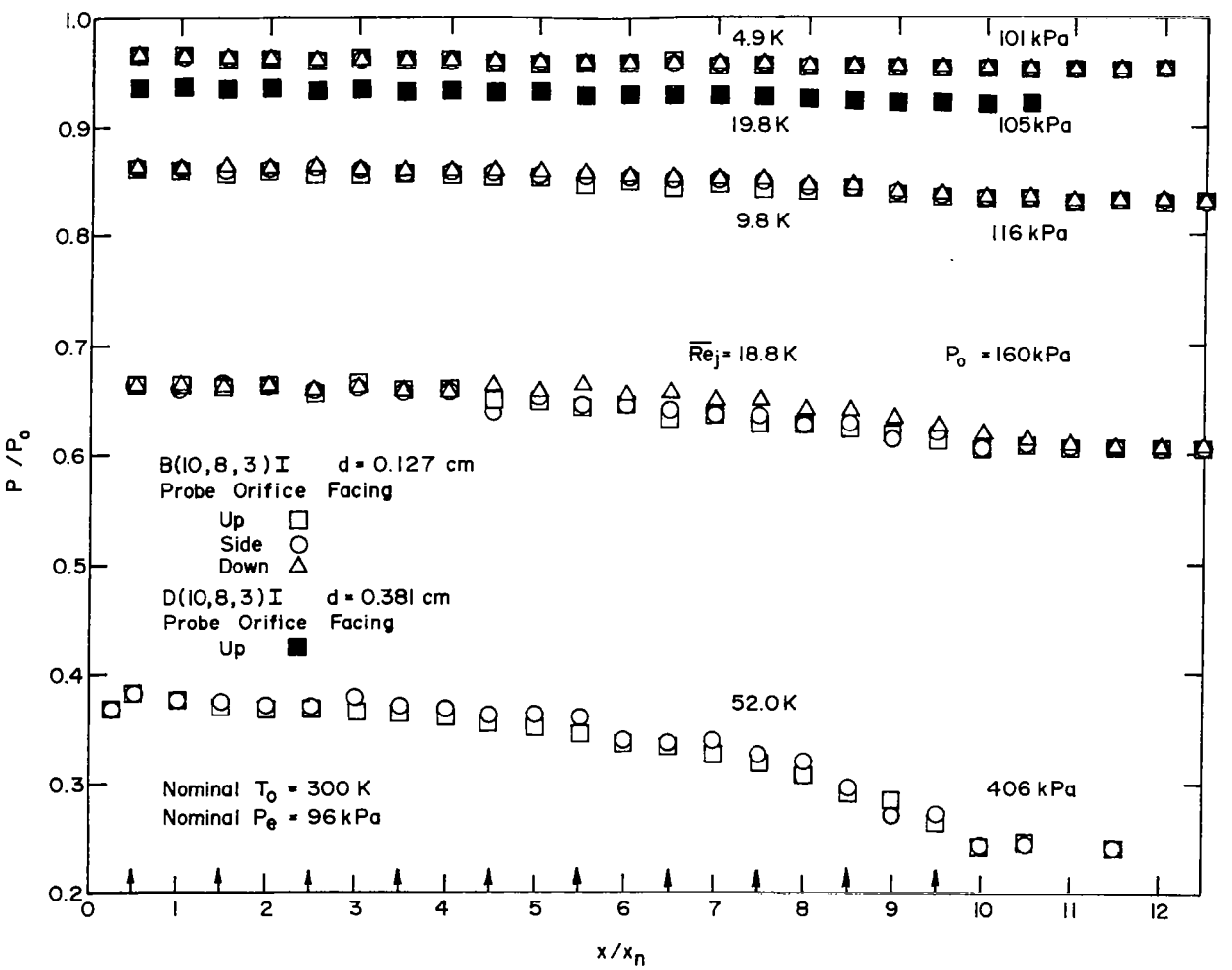

Fig. 3.1 Channel pressure traverses for (10,8,3)I geometry.

ratio, P/P_o, decreases significantly with increasing $\overline{Re}_j$. For $\overline{Re}_j$ = 52K, the pressure ratio across all holes is below the critical value for isentropic, one-dimensional flow of air, 0.53, indicating the flow is choked across all holes. The effect of hole diameter is indicated by comparing the results for the geometrically similar larger size case, D(10,8,3)I, at the nominal $\overline{Re}_j$ of 19K. The pressure ratio is significantly increased with increasing hole diameter.

Comparable B-size results, but for the narrow channel height of z/d = 1, are plotted in Fig. 3.2 for the up-facing probe orifice traverses. Here the pressure gradients along the channel are larger, with a smaller fraction of

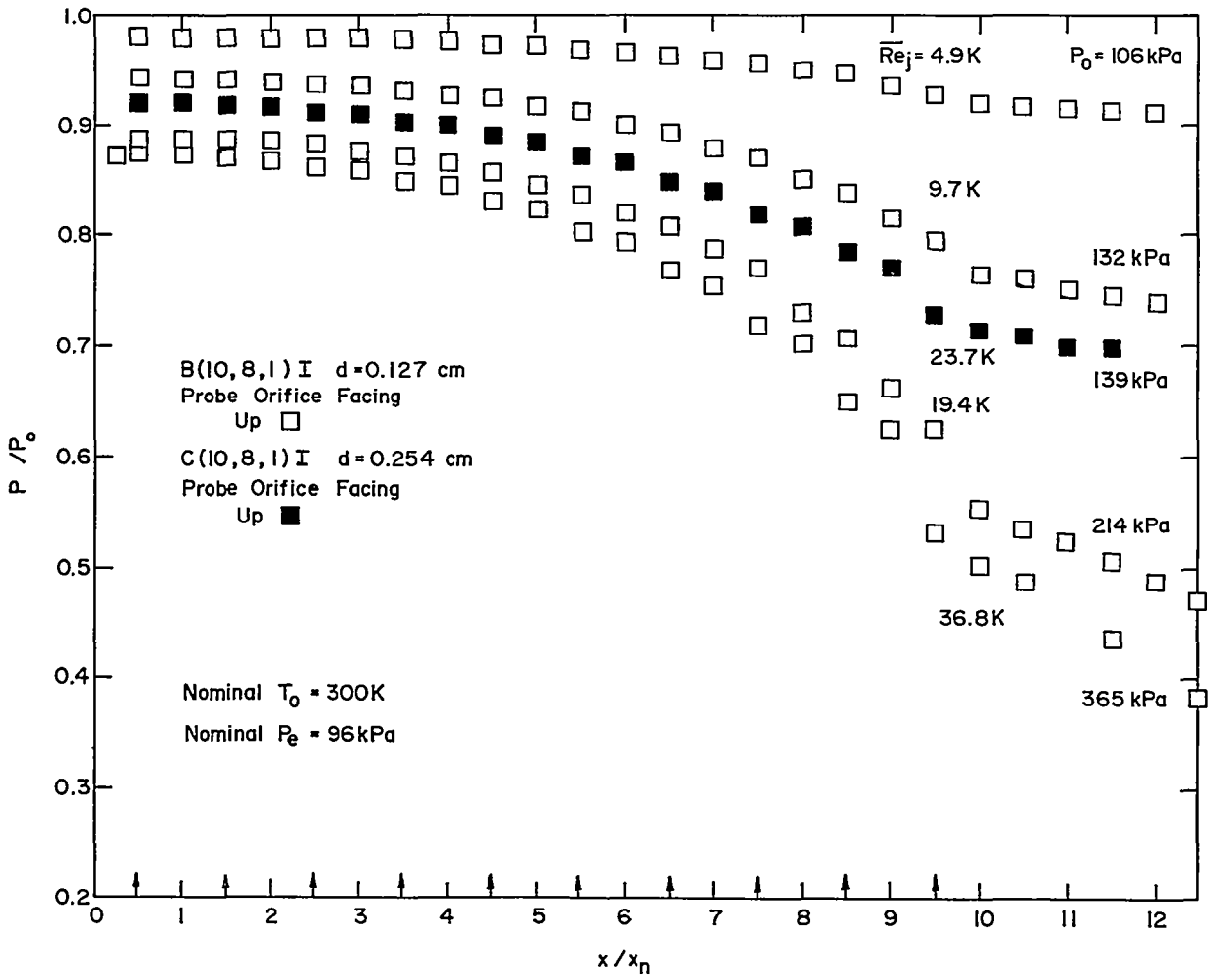

Fig. 3.2 Channel pressure traverses for (10,8,1)I geometry.

the pressure drop occurring across the holes than in the z/d = 3 case of Fig. 3.1. The pressure ratio is less sensitive to increases in flow rate (as reflected by $\overline{Re}_j$). The flow is just approaching a choked condition at the last (tenth) row of holes for the largest $\overline{Re}_j$ = 36.8K. The effect of hole diameter is again evident by comparing the C(10,8,1)I profile.

A final illustration of pressure traverse results is shown in Fig. 3.3 for two A-size configurations, A(10,8,3)I and A(10,6,2)S. Traverses for z/d = 1 in A-size were not obtained because the narrow channel height required such a small diameter probe that the orifice diameter required in the side wall of the probe would have been excessively small. In Fig. 3.3, the A(10,8,3)I configuration is choked across all holes at $\overline{Re}_j$ = 21K (compare

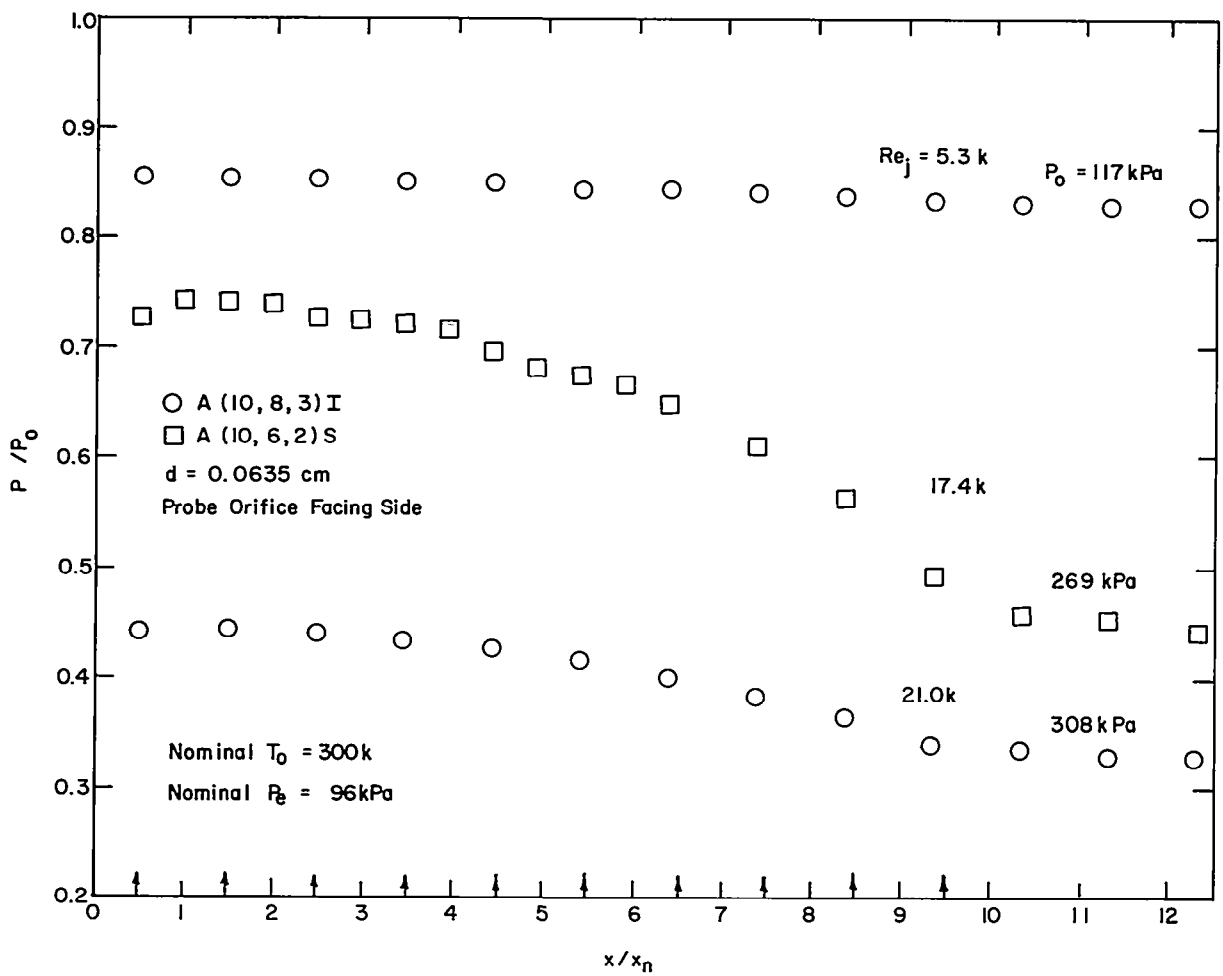

Fig. 3.3 Channel pressure traverses for two A-size geometries.

Fig. 3.1), and the A(10,6,2)S configuration shown for $\overline{Re}_j$ = 17.4K apparently becomes choked at the last row of holes.

It should be emphasized that the choked flow conditions occurred only for the smaller hole diameters at the larger jet Reynolds numbers. This results from the low laboratory pressure levels and the resulting relatively large pressure drops required for these cases. The effects of these conditions on the heat transfer coefficients were noted in a previous report [2] and will be referred to again in the heat transfer and correlation sections of this report.

A discharge coefficient for each jet plate was determined from a separate test conducted with the plenum/jet plate assembly removed from the test plate unit and discharging directly to the laboratory environment at atmospheric pressure. Plenum pressure and temperature were measured to calculate the ideal flow rate, assuming one-dimensional isentropic compressible flow, while the actual flow rate was determined via the standard sharp edge orifice in the flow metering section upstream of the plenum. Discharge coefficients were measured over a range of Re_j spanning that for which data was obtained in the heat transfer tests. In most cases at least 16 points were taken spread over the necessary range. The results for jet plate B(5,8)I for which the largest number of points was taken are shown in Fig. 3.4. These C_D values are

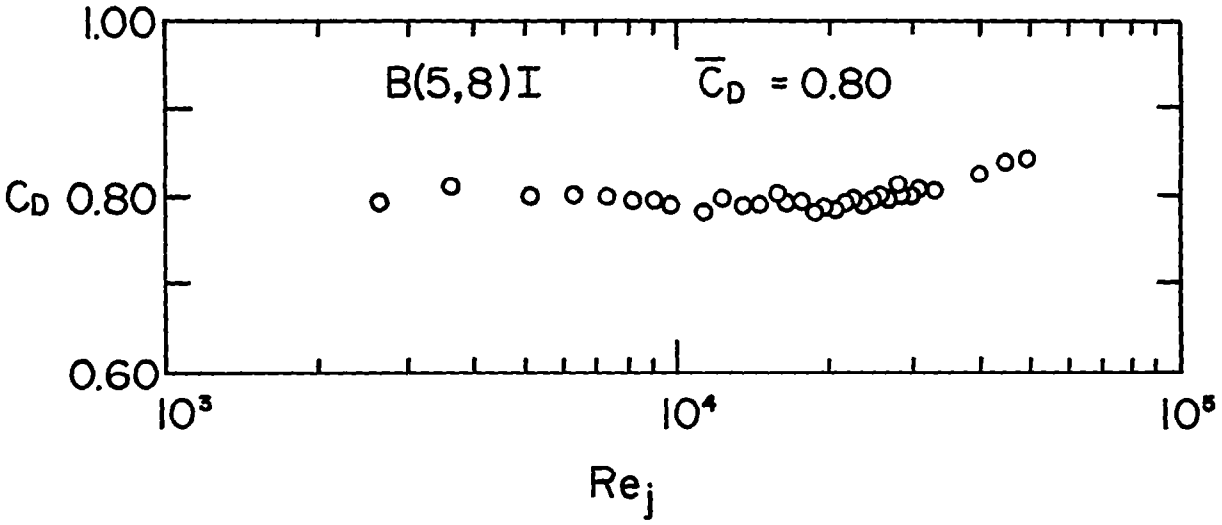

Fig. 3.4 Jet plate discharge coefficient as a function of jet Reynolds number.

essentially independent of Re_j over the range $2.5x10^3$ to $5x10^5$. The mean values of C_D for each jet plate are listed in Table 2.1. These values were used in determining the flow distributions. While discharge coefficients for individual holes were not determined, each jet plate was checked for flow uniformity with very satisfactory results as detailed in [2].

3.2 Flow Distribution Results

The distribution of the jet flow as calculated from the pressure traverse and discharge coefficient results is illustrated by the data points plotted in Figs. 3.5, 3.7, and 3.8. The ordinate, $G_j/\bar{G}_j$, represents the jet mass velocity for the individual spanwise rows normalized by the mean of the individual values over all ten rows. The points for the crossflow parameter, G_c/G_j, corresponding to those for $G_j/\bar{G}_j$ in Fig. 3.5, are plotted in Fig. 3.6 [excepting the C(5,6,1)I case, omitted for clarity]. The crossflow velocity, G_c, immediately upstream of a given row was determined by summing the individual row jet flow rates upstream of that row. In these Figures the vertical arrows along the abscissa indicate the row locations. Results are included for various mean jet Reynolds numbers and configuration sizes, and span the range of geometric parameter values. For ten of the twelve cases shown in these Figures the sum of the flow rates over all rows closed to within 3% or better of the total flow rate measured upstream of the plenum. For the remaining two cases one closed within 4%, the other within 6%. The better mass closures tended to occur for the higher flow rates for which the pressure drops across the holes were larger.

The curves in these Figures are based on the one-dimensional model presented in the next sub-section. The agreement is quite satisfactory. Some flow distribution test results obtained exhibited less precise and consistent agreement with the model than those displayed in Figs. 3.5 through 3.8. In general, however, the mass closures were also less satisfactory for such cases indicating increased uncertainty associated with the pressure traverses. The model leads to the result that the flow distribution is independent of the streamwise hole spacing, x_n/d, depending, for a given discharge coefficient and number of rows, only on the geometric parameter $(y_n/d)(z/d)$. This result

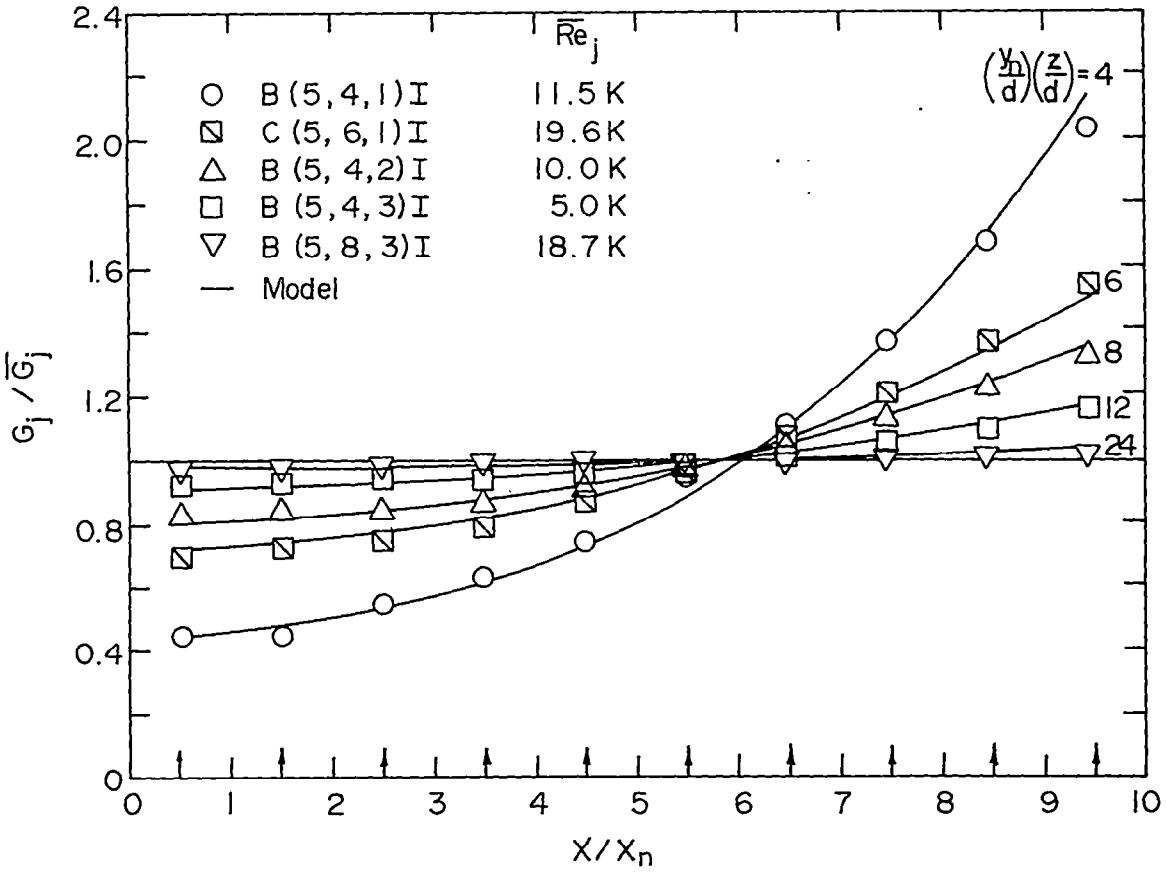

Fig. 3.5 Streamwise distribution of jet velocities—
Comparison between measured values and model, Eq. (3.7).

is corroborated by the data of Figs. 3.5 through 3.7. The range of this parameter covered in Figs. 3.5 and 3.6 matches that for the heat transfer tests. For the largest value, 24, the distribution is essentially uniform (Fig. 3.5) with a corresponding linear increase in the crossflow parameter, G_c/G_j (Fig. 3.6). For the smallest value, 4, the distribution is highly nonuniform with the jet velocity as small as one-half the mean at the first row, and as large as twice the mean at the tenth row; G_c/G_j increases linearly upstream but levels off quickly downstream to a maximum value of about 0.75.

The streamwise flow distributions are also independent of whether the hole pattern is inline or staggered as indicated by Fig. 3.8. This Figure includes a comparison for the (5,4,3) configuration. This configuration, with the smallest hole spacings and largest channel height, exhibited the most

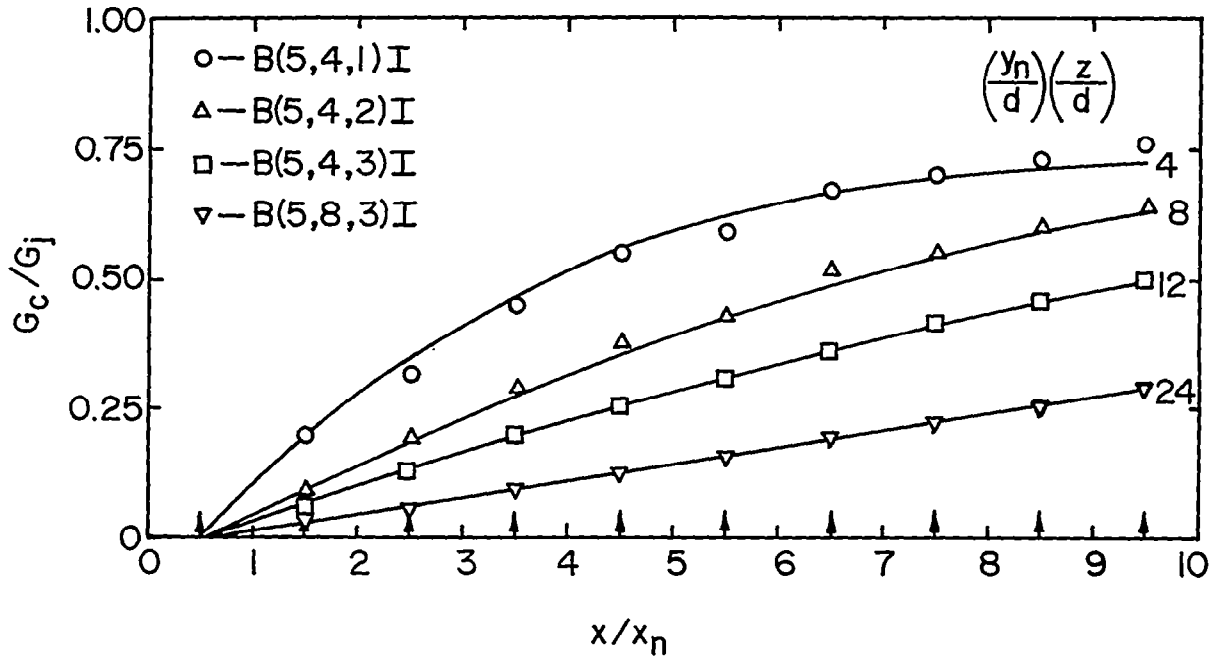

Fig. 3.6 Streamwise distribution of crossflow-to-jet velocity ratio—Comparison between measured values and model, Eq. (3.8).

significant differences in heat transfer coefficients of all configurations tested, when inline and staggered hole patterns were compared [2,3,4]. These differences cannot be attributed to differences in individual spanwise row jet Reynolds numbers because the streamwise flow distributions are the same (Fig. 3.8). Rather, as previously discussed [2,3], it is suggested that the observed differences in heat transfer coefficients are due to differences in the spanwise distribution of the crossflow which develop as one proceeds downstream along the channel. This point will again be referred to in the heat transfer and correlation sections of this report.

3.3 Flow Distribution Model

The discrete hole array is imagined to be replaced by a surface over which the injection is continuously distributed (Fig. 3.9). The jet velocity G_j is related to the continuously distributed injection velocity G_j^* through the open area ratio, $G_j^* = G_j A_o^*$. Thus, assuming incompressible flow, the

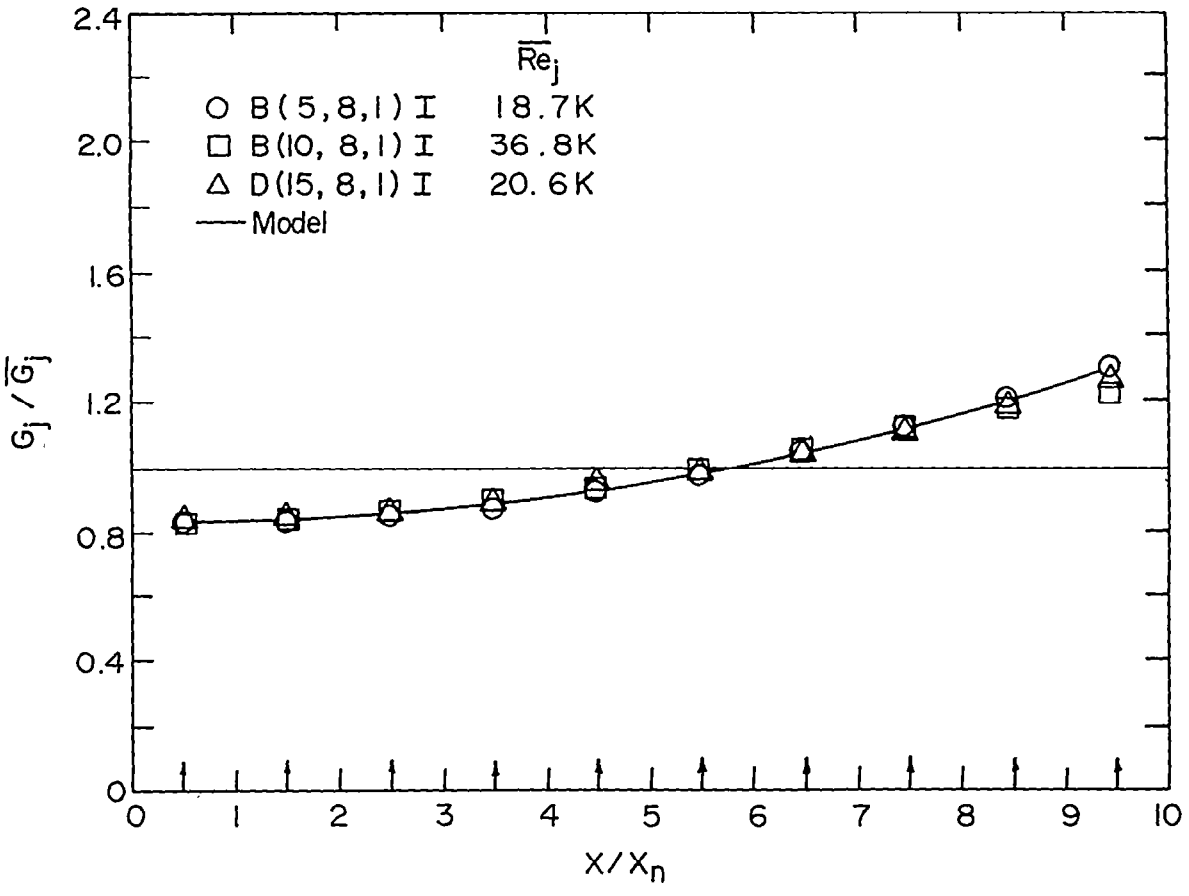

Fig. 3.7 Effect of streamwise hole spacing on streamwise distribution of jet velocities.

distributed injection velocity may be written in terms of the discrete hole discharge coefficient as

$$G_j^* = A_o^* C_D [2\rho(P_o - P)]^{1/2} \tag{3.1}$$

The streamwise pressure gradient in the channel is assumed to be primarily due to the acceleration of the flow caused by the injected fluid, with negligible influence of the wall shear. Accordingly, a force-momentum balance on the control volume indicated in Fig. 3.9a results in

$$dP = - \frac{2G_c dG_c}{\rho} \tag{3.2}$$

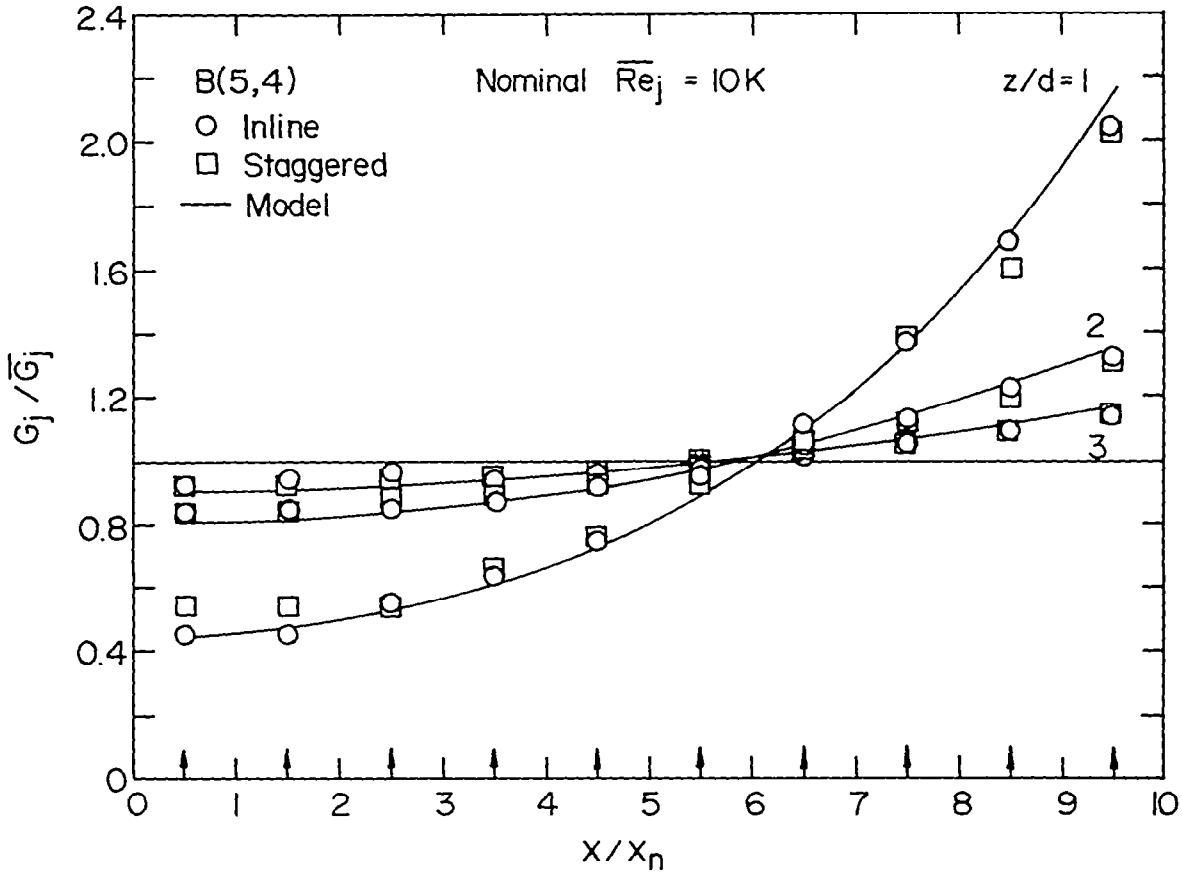

Fig. 3.8 Effect of inline vs. staggered hole pattern on streamwise distribution of jet velocities.

A mass balance leads to

$$G_j^* = z \frac{dG_c}{dx} \tag{3.3}$$

For constant C_D and P_o, the elimination of G_j^* and P from (3.1), (3.2), and (3.3) in favor of G_c yields

$$\frac{d^2G_c}{dx^2} - M^2G_c = 0 \tag{3.4}$$

where $M = \sqrt{2}\, A_o^*\, C_D/z$. The upstream boundary condition is $G_c = 0$ at $x = 0$. A second boundary condition results from an overall mass balance for a channel length L written in terms of the overall mean injection velocity; i.e., $G_c = \overline{G}_j^* L/z$ at $x = L$. Integration of (3.4) then gives

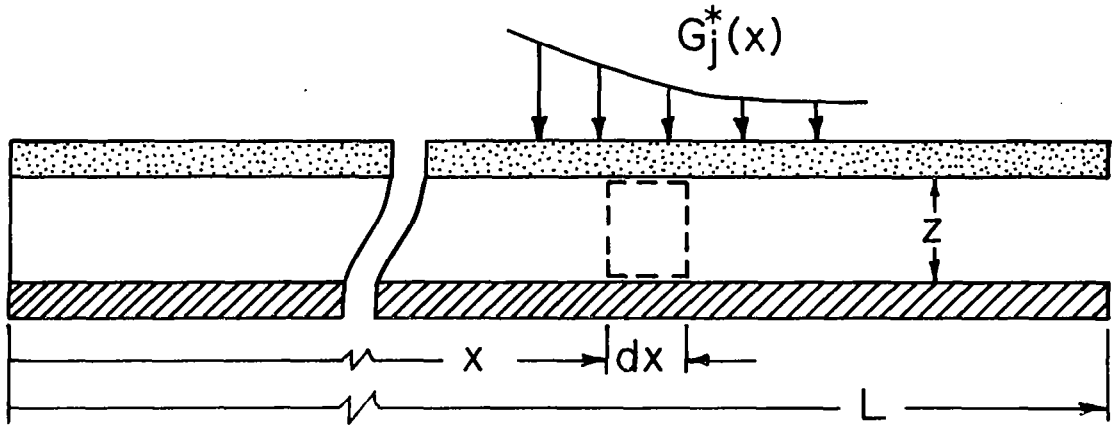

Fig. 3.9a Continuous injection model.

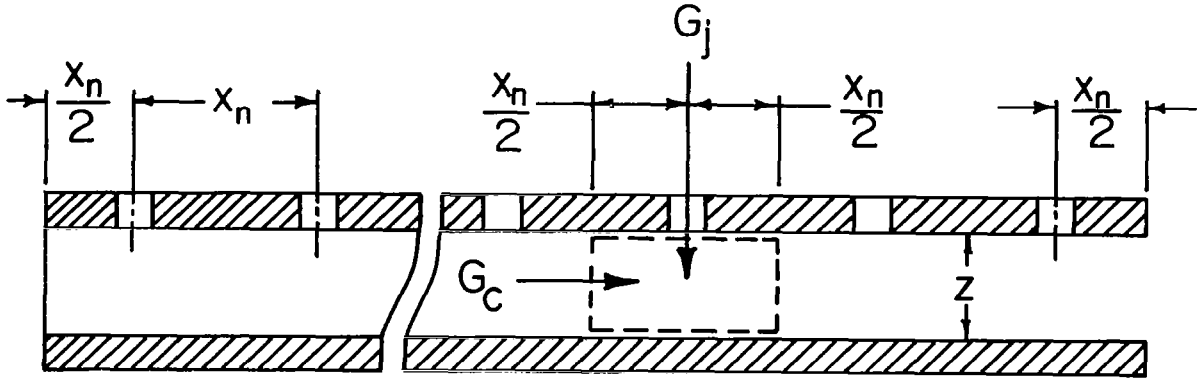

Fig. 3.9b Discrete hole injection model.

$$\frac{G_c}{\overline{G}_j^*} = \frac{L}{z}\,\frac{\sinh Mx}{\sinh ML} \tag{3.5}$$

for the crossflow distribution. The corresponding injected flow distribution obtained from (3.3) with the aid of (3.5) is given by

$$\frac{G_j^*}{\overline{G}_j^*} = \frac{ML\cosh Mx}{\sinh ML} \tag{3.6}$$

The discrete hole array jet velocity distibution is determined from (3.6) by assuming that the value of G_j for a given spanwise row of holes is that corresponding to $G_j^*(x)$ with x evaluated at the centerline of the row. For the uniform rectangular arrays of interest here $A_o^* = (\pi/4)/[(x_n/d)(y_n/d)]$, $L = x_n N_c$, and the first row is at $x = x_n/2$. Noting also that $\overline{G}_j^* = \overline{G}_j A_o^*$, the jet velocity distribution based on (3.6), may be written as

$$\frac{G_j}{\overline{G}_j} = \frac{\beta N_c \cosh \beta(x/x_n)}{\sinh \beta\, N_c} \tag{3.7}$$

where

$$\beta = C_D\sqrt{2}(\pi/4)/[(y_n/d)(z/d)]$$

and

$$x = x_n(i-1/2) \qquad i = 1,2,3\ .\ .\ .N_c$$

Besides the jet array velocity distribution given by (3.7), an additional flow parameter relevant to the correlation of the streamwise resolved heat transfer coefficients is the ratio of the crossflow velocity immediately upstream of a given spanwise row to the jet velocity of that row. This may be satisfactorily approximated utilizing G_c from (3.5) evaluated one-half a hole spacing upstream of the given row (Fig. 3.9b), divided by G_j from (3.7). This results in

$$\frac{G_c}{G_j} = \frac{1}{\sqrt{2}\,C_D}\,\frac{\sinh \beta(x/x_n-1/2)}{\cosh \beta(x/x_n)} \tag{3.8}$$

where the spanwise hole row locations are the same as previously indicated following (3.7).

The curves shown in Figs. 3.5, 3.7, and 3.8, previously discussed, are based on Eq. (3.7). Those shown in Fig. 3.6, also previously discussed, are based on Eq. (3.8).

The model developed above is similar to that presented by Martin [11] for an array of slot nozzles in which the outlet flow is constrained to exit parallel to the slots. The present results, as illustrated by Figs. 3.5 through 3.8, indicate the applicability of this type of model for discrete hole arrays as well, at least over the range of parameters covered by the test program.

Though the model is based on the assumption of an incompressible flow, Eqs. (3.7) and (3.8) apply satisfactorily for the present geometries even when pressure ratios are such that the flow is choked across the holes or nearly so. This occurred only for geometries having the largest spanwise spacings and channel heights, $(y_n/d, z/d) = (8,3)$, and then only for the larger flow rates and smaller hole diameters. In these cases the jet flow distribution predicted by the model is uniform [Fig. 3.5, $(y_n/d)(z/d) = 24$] to within a few percent. Thus, it essentially matches the uniform experimentally determined distributions which result when the flow is choked across all the holes.

4. HEAT TRANSFER COEFFICIENTS

Both mean and streamwise resolved heat transfer coefficients for jet plate configurations summarized in Table 2.1 were previously presented and discussed as a function of mean jet Reynolds number and geometric parameters [2,3,4]. Heat transfer coefficients resolved to one or two streamwise hole spacings [2,4] and to one-third the streamwise hole spacing [2,3] were considered. The heat transfer test plate (impingement surface) was isothermal. Experimental procedures and data reduction techniques were outlined in [4] and were further detailed in [2], which includes a complete tabulation of mean and resolved Nusselt numbers. In reducing the data, the resolved heat transfer coefficients were defined in terms of the difference between the impingement surface temperature, T_s, and the corresponding adiabatic wall (recovery) temperature, T_r. This was essential in determining heat transfer coefficients from the test results, since for some geometries, especially at the higher flow rates, the difference between T_r and the plenum air temperature, T_o, was quite significant compared with the surface-to-plenum air temperature differences $(T_s - T_o)$ at which the tests were conducted (normally 15 to 30K). For the gas turbine application, however, conditions are such that one may take $T_r \cong T_o$, since $(T_r - T_o)$ is negligible compared with $(T_s - T_o)$. Therefore, knowledge of the heat transfer coefficient and the surface and plenum temperatures is adequate for calculating heat fluxes in this anticipated application of these results.

The present objectives are to examine the heat transfer coefficients resolved to one streamwise hole spacing as a function of the associated spanwise row jet velocity, crossflow velocity, and geometric parameters; and to achieve a correlation in terms of these quantities. Thus, we consider

$$h = f(G_j, G_c, x_n, y_n, z, d)$$

or in dimensionless form, taking account also of relevant fluid properties,

$$Nu = f(Re_j,\ G_c/G_j,\ Pr,\ x_n/d,\ y_n/d,\ z/d) \qquad (4.1)$$

Since the flow distribution model presented in the previous section was well supported by the flow distribution data, this model was used for

determination of Re_j and G_c/G_j. It should be emphasized, however, that only the distribution of Re_j relative to the mean, i.e., $Re_j/\overline{Re}_j = G_j/\overline{G}_j$ was determined from (3.7). The mean values were taken from the sharp-edge orifice total flow rate measurements upstream of the plenum since they are more accurate than the sum of the individual row flow rate measurements.

The maximum nominal range of $\overline{Re}_j$ for which heat transfer data was obtained was $5x10^3$ to $5x10^4$, though the full range was not covered for every individual geometry. Considering the geometries with the most highly nonuniform flow distribution, $(y_n/d)(z/d) = 4$, the maximum nominal range of Re_j was $2.5x10^3$ to $1.75x10^4$ for Row 1 ($G_c/G_j = 0$) and 10^4 to $7x10^4$ for Row 10 ($G_c/G_j \cong 0.75$). For the most nearly uniform flow conditions, $(y_n/d)(z/d) = 24$, the Re_j range for all rows ($0 \leq G_c/G_j \leq 0.28$) was essentially the same as the range for $\overline{Re}_j$.

Normally, for a given configuration, heat transfer coefficients were obtained for three values of $\overline{Re}_j$ over its range. However, in some cases data were obtained at four or five values while for a few of the C-size geometries data were taken at just two values. Least squares power function fits of the form $Nu = A\,Re_j^m$ were applied separately to individual data sets, with A and m permitted to be adjustable constants for each set. A data set for this purpose consisted of the measured Nu values at each Reynolds number for a given geometric size, $(x_n/d, y_n/d, z/d)$, hole pattern, and spanwise row. Ninety-five percent of the data points deviated from these fit lines by less than 3%, 99% by less than 4%, and 100% by less than 9%, which compares quite favorably with the estimated uncertainty for the Nu data which was $\pm 5\%$ for 95% confidence [2]. Thus, the confidence which may be placed in interpolated data points based on these individual fits may be considered as good as that for the original data points. Results based on these fits were used in examining the effects of geometric parameters and crossflow at fixed values of Re_j as discussed in the paragraphs below.

Examination of Fig. 4.1* indicates that Nu_1, for which $G_c/G_j = 0$, decreases significantly with both x_n/d and y_n/d for fixed Re_j. The points

*The points for each specific hole spacing combination (x_n/d, y_n/d) are drawn from the same geometric sizes (B, C, or D) identified in Fig. 4.2.

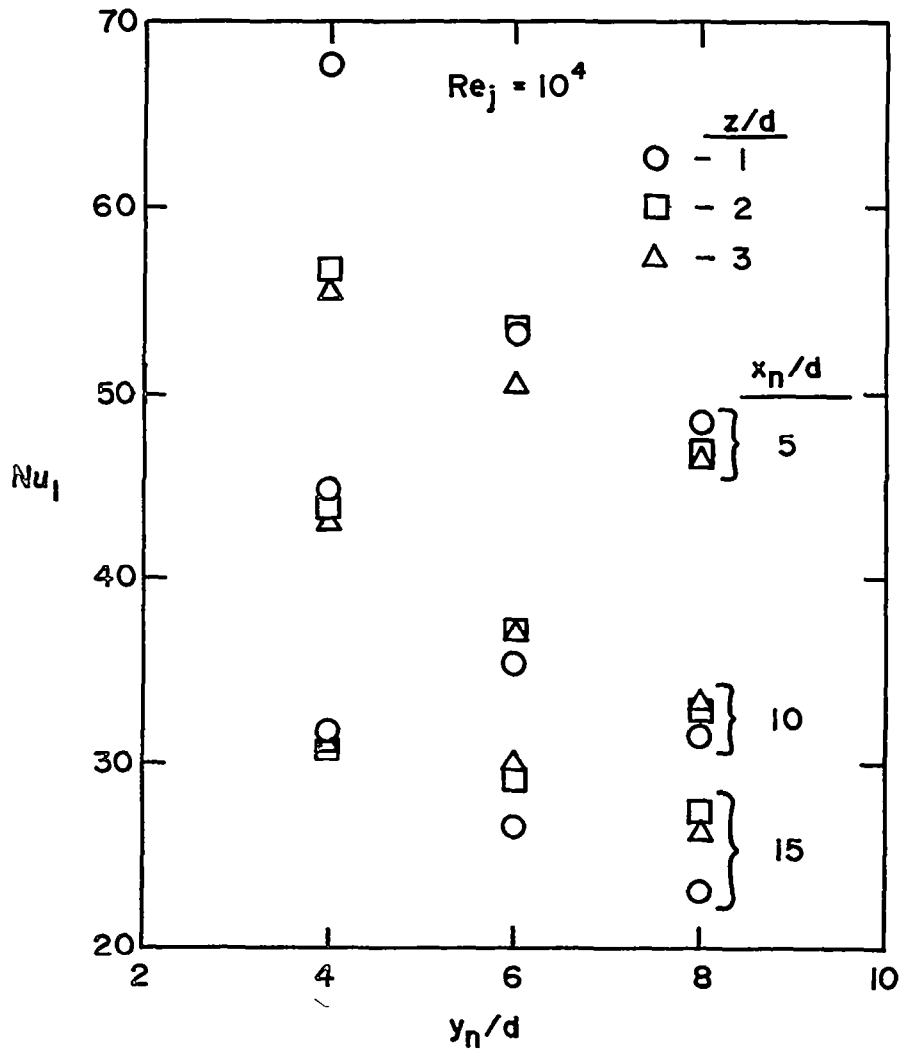

Fig. 4.1 Effect of geometric parameters on Nusselt number for initial upstream row of array ($G_c/G_j = 0$). Inline hole pattern.

shown are for $Re_j = 10^4$; however, the trend with geometric parameters is similar over the Re_j range of the tests. The sensitivity to z/d is quite small except for the highest hole density configuration, $(x_n/d, y_n/d) = (5,4)$, where Nu_1 for z/d = 1 is significantly larger than the values for z/d = 2 and 3. This is not a spurious data point because the data for the corresponding geometrically similar sizes corroborate this behavior. The trend of Nu_1 with z/d is decreasing for small values of x_n/d and y_n/d, but increasing for large values. This type of behavior tends to work against development of a tight correlation of simple form.

4.1 Effect of Crossflow

The matrix of plots in Fig. 4.2 shows the effect of the crossflow parameter, G_c/G_j, on Nu where Nu is normalized by Nu_1. Each plot presents results for z/d = 1,2, and 3 for a single hole spacing combination (x_n/d, y_n/d). The data shown in each plot are for the smallest geometric size tested for that combination (excluding A-size for which Nu could not be resolved to one streamwise spacing). All points are for $Re_j = 10^4$ but in this normalized form are representative of the general trends over the full Re_j range.

The trend of Nu/Nu_1 with G_c/G_j shifts from a monotonic decreasing function to a form which exhibits a broad minimum as x_n/d and y_n/d increase, and as z/d decreases. Thus, for $x_n/d \geq 10$, $y_n/d \geq 6$, z/d = 1, and $G_c/G_j \gtrsim 0.4$, Nu/Nu_1 increases slowly. A plausible explanation for this behavior, consistent with the fact that it occurs for large hole spacings and small channel heights, is that the crossflow provides an increasingly significant direct contribution to the heat transfer rate but does not cause a large degradation in the direct contribution from jet impingement. It may be remarked that results for heat transfer coefficients resolved to better than one streamwise hole spacing indicate that for these geometries the jets still impinge on the surface at the final downstream row; and, indeed, the impingement point is deflected downstream only a small fraction of the hole spacing [2,3]. This inference is further corroborated by observations of discoloration patterns made subsequent to these test runs on the copper heat transfer surface. These observations clearly indicate impingement of all jets with only slight deflection even at the final downstream row. In contrast, for smaller hole spacings and/or larger channel heights the jets are deflected and diffused more by the crossflow, and though they still impinge on the heat transfer surface, their cooling effectiveness is more significantly reduced. At the same time there is less surface area available for direct cooling by the crossflow.

The effect of increasing z/d, where significant, is to decrease Nu/Nu_1 at fixed G_c/G_j. This trend is consistent with the results of Metzger and Korstad [12] for a single row of jets tranverse to a crossflow. The sensitivity of

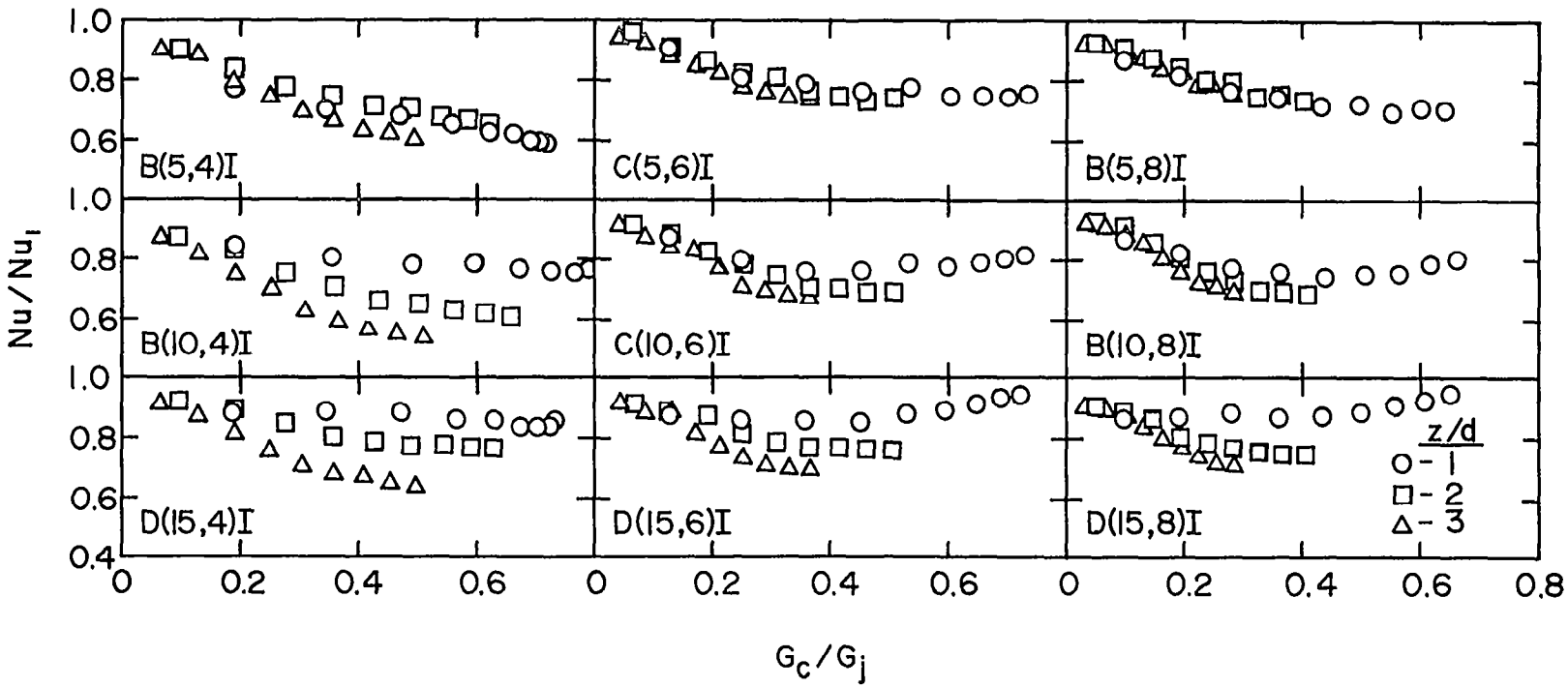

Fig. 4.2 Effect of crossflow and geometric parameters on streamwise resolved Nusselt numbers emphasizing effect of z/d. Inline hole pattern.

Nu/Nu_1 vs G_c/G_j to z/d increases with x_n/d but decreases with y_n/d. Thus, the effect of z/d is significant for $(x_n/d, y_n/d) = (15,4)$, the lower left plot, but essentially disappears for (5,8), the upper right plot. Or, stated another way the sensitivity of the crossflow effect to z/d appears to increase as the aspect ratio x_n/y_n increases. The complexity of the interacting jet/crossflow phenomena in the two-dimensional array precludes arriving with high confidence at a particular explanation, at least on the basis of currently available information. However, it may be appropriate to note several factors which contribute to the complexity, and may be involved in potential explanations.

First, the crossflow velocity appearing in the crossflow parameter G_c/G_j as used in characterizing the present results is a mean value over the channel cross-section. Consider the distribution across the channel span of the crossflow velocity averaged over the channel height. There is some evidence, e.g., flow visualization, indicating that for the inline arrays the crossflow tends to become channelized between adjacent streamwise jet rows. Thus, the spanwise flow distribution would be nonuniform with velocities between jets larger than those directly approaching the next downstream jet. The degree of nonuniformity would vary with array geometric parameters. Thus, the crossflow velocity immediately upstream of a given jet in an array would be smaller than the mean velocity over the cross-section by differing amounts depending on array geometry. Heat transfer coefficients obtained during preliminary tests with a spanwise uniform initial crossflow approaching the array were smaller than those measured following a certain downstream location for the same array without <u>initial</u> crossflow, but with total upstream jet flow rate adjusted so as to provide the same value of G_c/G_j approaching the downstream location.

Second, the values of Nu being compared for various $(x_n/d, y_n/d)$ combinations are averages over rectangles of widely varying aspect ratios, from $x_n/y_n = 0.625$ for the (5,8) case where no z/d effect is apparent to 3.75 for the (15,4) case where the effect is significant.

Third, results for potential core length obtained by Stoy and Ben-Haim [15] for a single jet in a confined crossflow indicate that for the present range of z/d, impingement may occur for certain jets before they are developed, and for others (even in the same array) after they are developed.

The identical data points plotted in Fig. 4.2 are replotted in Fig. 4.3, but rearranged with x_n/d rather than z/d as the parameter within each individual plot. At z/d = 1 the points for $x_n/d = 5$ fall below those for $x_n/d = 10$ which in turn fall below those for $x_n/d = 15$. On the other hand, for z/d = 2 and 3, points for $x_n/d = 5$ fall between or above those for $x_n/d = 10$ and 15 depending on the value of y_n/d. The amount of spread among the data points in each plot decreases with increasing y_n/d and z/d. Thus, the largest spread occurs for $(y_n/d, z/d) = (4,1)$, the upper left plot, while the spread nearly disappears for $(y_n/d, z/d) = (8,3)$, the lower right plot. Or, put another way, Nu/Nu_i is not sensitive to x_n/d when y_n/d and z/d are large, but is sensitive when they are small.

4.2 Effect of Hole Pattern

This effect is illustrated in Fig. 4.4 where Nusselt numbers for staggered hole patterns normalized by those for their counterpart inline patterns are plotted against the crossflow parameter. The effect is not significant for the largest hole spacing, $(x_n/d, y_n/d) = (10,8)$. However, as x_n/d and y_n/d decrease, and as z/d increases, the staggered pattern results in increasingly reduced heat transfer coefficients relative to the inline values for increasing crossflow.

This behavior is thought to be associated with differences in spanwise distribution of the crossflow in the two cases [2,3]. The tendency of the crossflow to become channelized between adjacent streamwise rows of the inline pattern reduces the direct influence it can exert on each downstream jet. In contrast, the spanwise crossflow distribution presumably remains more nearly uniform for the staggered patterns; hence the crossflow approach velocity directly upstream of each jet is somewhat larger than for the matching inline case.

4.3 Effect of Jet Plate Thermal Boundary Condition

Throughout the major heat transfer test program an isothermal boundary condition was utilized at the impingement surface. In general, no provision

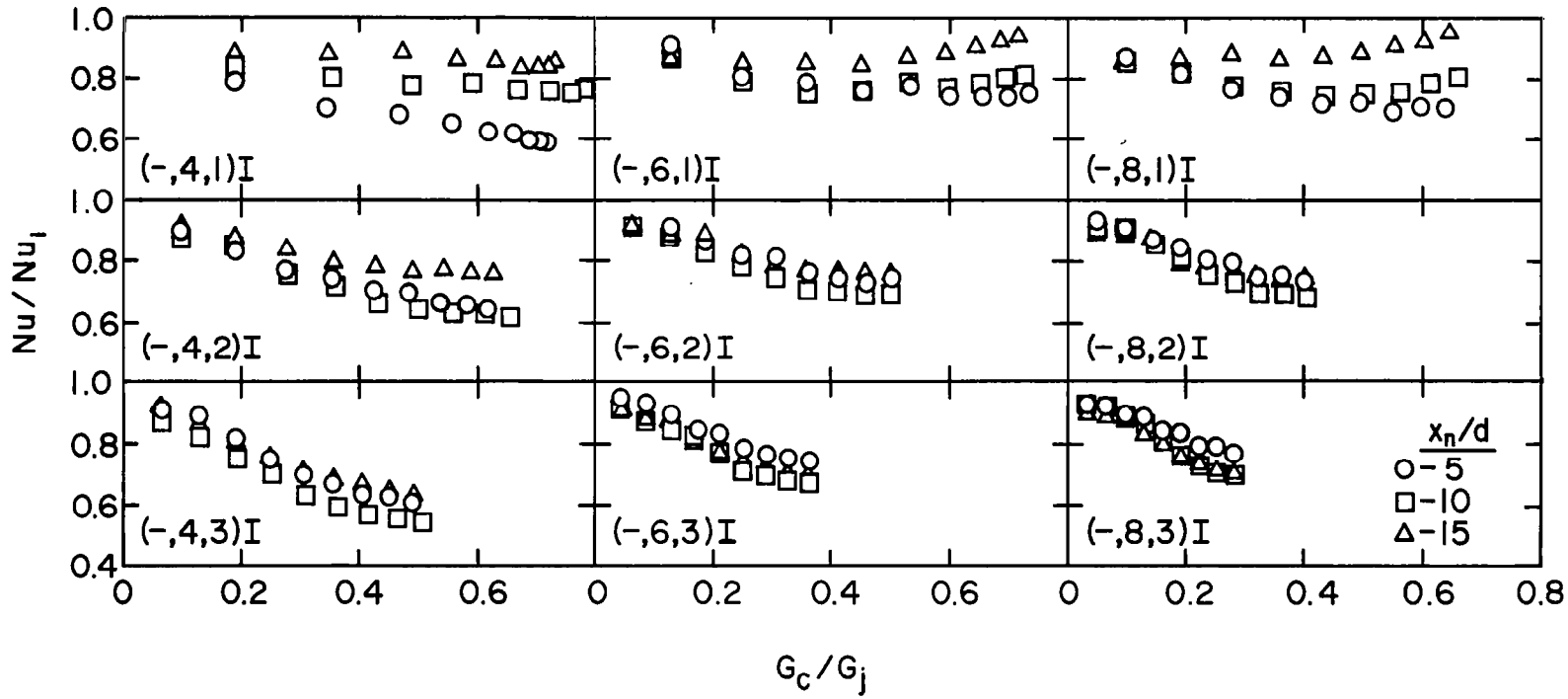

Fig. 4.3 Effect of crossflow and geometric parameters on streamwise resolved Nusselt numbers emphasizing effect of x_n/d. Inline hole pattern.

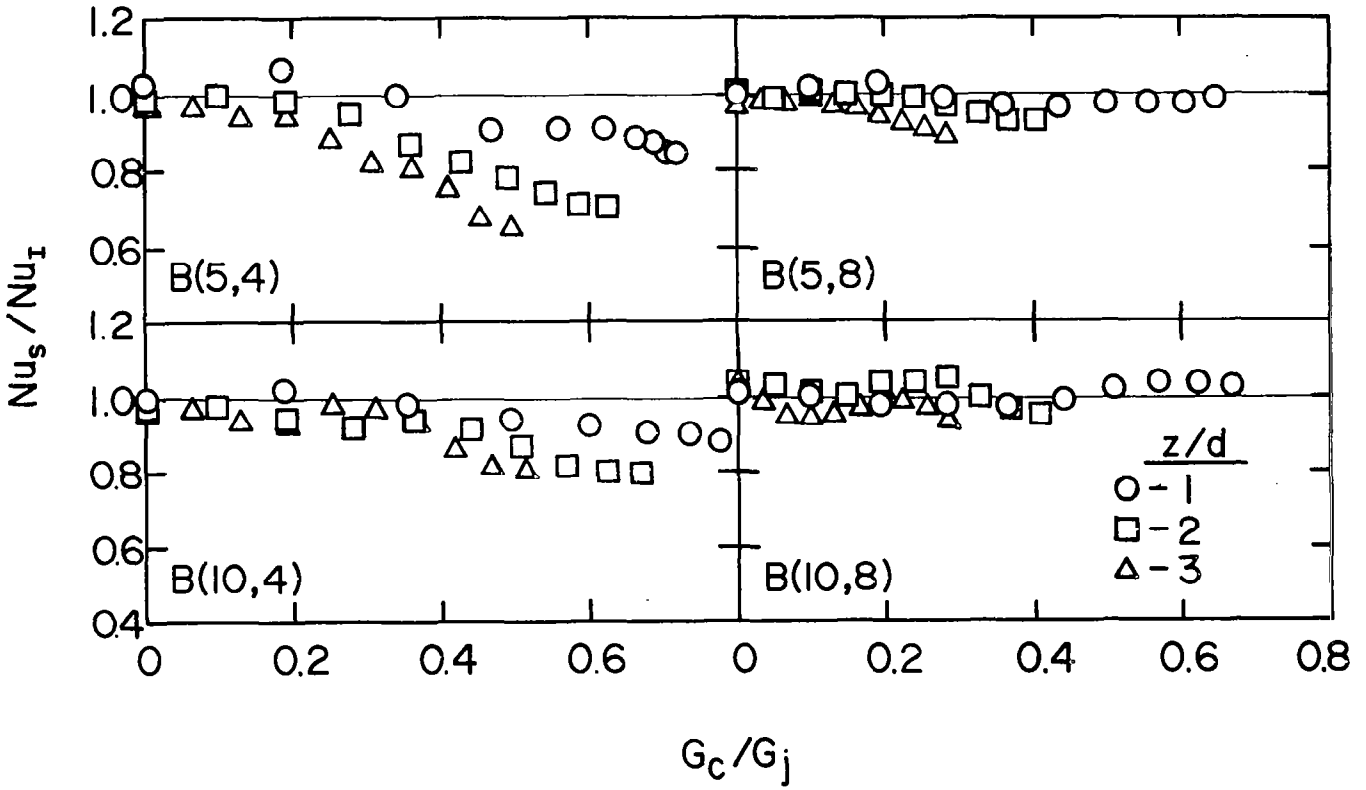

Fig. 4.4 Effect of hole pattern (staggered vs. inline) on streamwise resolved Nusselt numbers as function of crossflow and geometric parameters.

was made to idependently control the thermal boundary condition at the exit plane of the jet plate; i.e., the channel wall opposite the impingement surface. It was not expected that this boundary condition would significantly affect the heat transfer coefficients to be determined at the impingement surface. However, early in the program it was deemed wise to verify this expectation, particularly for the narrowest channel height of z/d = 1. Accordingly, jet plate A(10,8)I was fitted with resistance heating wires attached to and distributed uniformly over the plenum side of the plate. By adjusting the power input to this heating element the channel wall temperature at the exit plane of the aluminum jet plate could be controlled independently of the impingement surface and plenum air temperatures.

During the initial heat transfer tests conducted with jet plate A(10,8)I, mounted with a channel height z/d = 1, impingement surface heat transfer coefficients were measured (at each Reynolds number level) not only with zero power input to the jet plate heater (the reference or normal condition) but for two finite jet plate heater power input levels: one equal to the maximum power input to the impingement surface test plate heaters, and one equal to half that value. To within experimental uncertainty the impingement surface heat transfer coefficients were unaffected by the power input level to the jet plate heater element.

The special tests utilizing the jet plate heater were discontinued when the heat transfer measurements were made for this jet plate at z/d = 2 and 3, it being reasoned that if the effect discussed above were negligible for a channel height of 1 it would certainly be also for larger channel heights. However, the jet plate heater wires were left in place.

As the test program proceeded and heat transfer data for the larger B, C, and D sizes of the (10,8)I configuration became available, it was noted that the Nusselt numbers for the B, C, and D sizes, compared at the same mean jet Reynolds numbers, were, in general, more consistent with each other than with the corresponding A-size values. This was detailed in [2] (see, in particular, Fig. 4.5 of that report), where it was suggested that some differences observed at larger Reynolds numbers may be due to compressibility effects, while differences at smaller Reynolds numbers where compressibility

effects could not be a factor, may be due to effects of turbulence characteristics.

Subsequently, it was decided to rerun several of the A(10,8)I tests with the jet plate heater wires removed, motivated by the thought that the physical presence of these wires, originally installed for heating purposes, may be affecting the turbulence characteristics of the jets enough to cause observable effects on the heat transfer coefficients. Tests conducted at $z/d = 1$ and 3 with the heater wires removed gave results which, for $z/d = 1$, differed from the original A-size results but were now more consistent with the corresponding B, C, and D size results. For $z/d = 3$, the results were essentially unchanged.

It was then decided to run a series of comparative tests using the A(10,8)I jet plate with and without wires, now considered as roughness elements, in order to further characterize the effects of their presence, especially since the initially observed effect was to enhance the heat transfer. The results of this series of tests are detailed in the next section.

4.4 Effect of Roughness Elements on Plenum Side of Jet Plate

As indicated above a series of comparative tests was performed with and without roughness elements attached to the plenum side of the A(10,8)I jet plate. The detailed geometry and method of attachment of the elements for these tests was patterned after that of the original installation of heater wires on this jet plate, since it was the presence of these wires which lead to the initial observation of the effect in question. Strips of double-sided masking tape were placed between the streamwise rows of jet holes on the plenum side of the jet plate. A single 0.0254 cm (0.010 in.) diameter wire was placed along each strip positioned midway between adjacent rows. Strips of plastic tape were then pressed down tightly over the wires.

Heat transfer tests were run for $z/d = 1$, 2, and 3 at nominal mean jet Reynolds numbers of 5, 10, and 20K with the roughness elements in place, and with the elements removed. The results are compared in Fig. 4.5. Results for the cases with the elements removed are denoted as ''Standard,'' while those

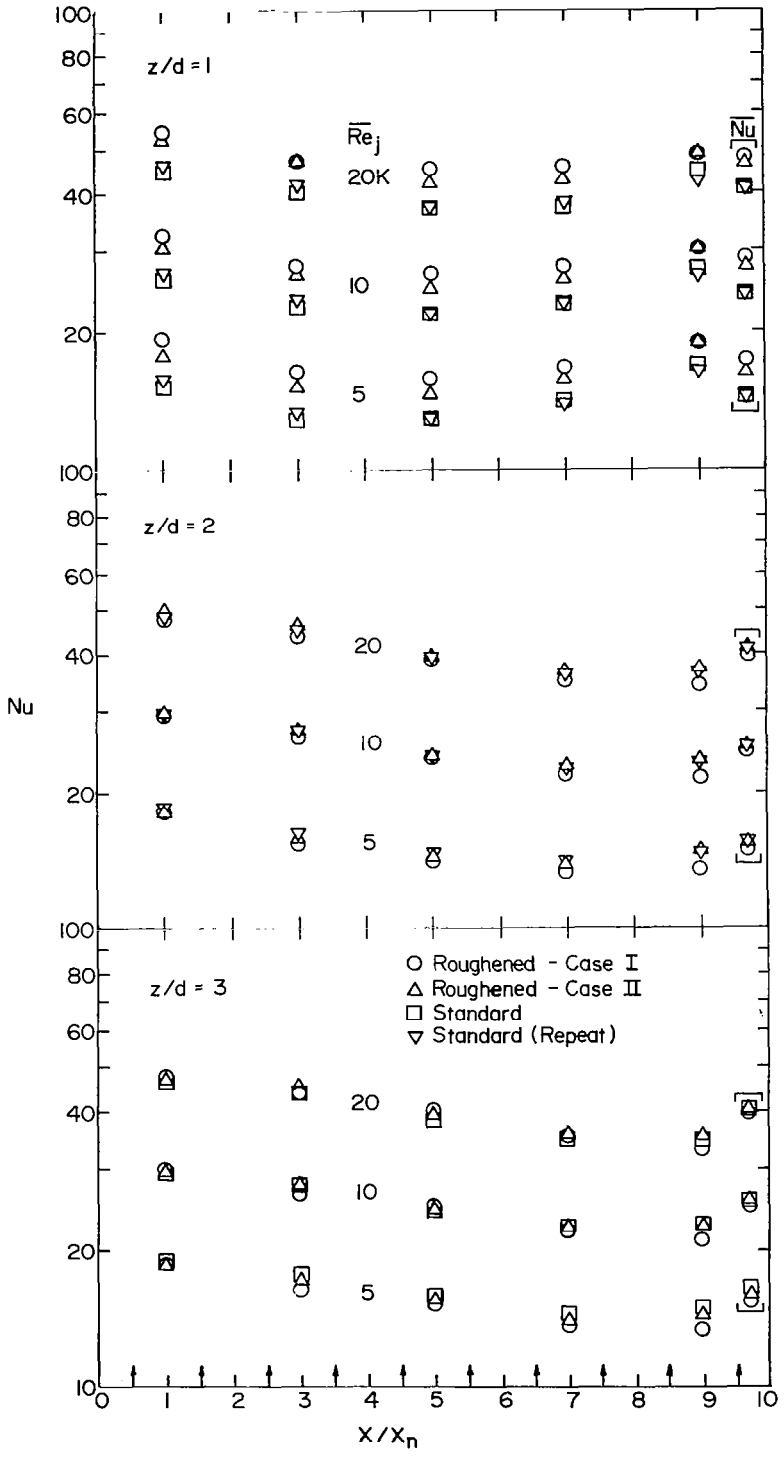

Fig. 4.5 Effect of jet plate plenum side roughness elements on Nusselt numbers for A(10,8)I configuration.

with the elements in place are denoted as ''Roughened—Case II.'' Results from the original A(10,8)I tests conducted when the original heater wires were in place are also included, denoted as ''Roughened—Case I.'' Overall there is little difference between the standard and roughened cases for z/d = 2 and 3. Most of the points are consistent to within experimental uncertainty. However, for z/d = 1 the Nusselt numbers for the roughened cases are uniformly higher than those for the standard case by about 15% over the entire Reynolds number range and at all positions along the impingement surface.

The A-size data for the standard case at z/d = 1 is also more consistent with the data for the geometrically similar B, C, and D size cases than is the data for the roughened cases. Deviations from least squares power function fit lines to the combined data of all four sizes for the (10,8)I configuration at z/d = 1 were summarized in Table 4.4 of a previous report [2]. The A-size data considered there was from the original tests with the heater wires in place (Roughened--Case I). The corresponding fit lines and deviations have since been recalculated with the A-size data replaced by that from the more recently obtained data for the standard A-size case (wires removed). The relevant portion of Table 4.4 from [2] is reproduced below with the revised deviations included in parentheses immediately following the corresponding original values. The improved overall consistency for z/d = 1 is reflected by

Sizes Included in Fits	z/d	Nusselt Number (Mean or Resolved)	Maximum Absolute Percent Deviation for Confidence Level of			Total Number of Points Involved
			95%	99%	100%	
A, B, C, D	1	$\overline{Nu}$	14(7)	14(7)	14(7)	13
		$Nu(2x_n)$	18(11)	26(11)	26(11)	65
	2	$\overline{Nu}$	11(9)	11(9)	11(9)	12
		$Nu(2x_n)$	13(12)	14(12)	14(12)	60
	3	$\overline{Nu}$	12(12)	12(12)	12(12)	13
		$Nu(2x_n)$	12(12)	16(16)	16(16)	65

the significantly reduced deviations. The consistency for z/d = 2 and 3 where the presence or absence of the wires had little effect remains essentially unchanged.

Gardon and Akfirat [17] observed a significant increase in stagnation point heat transfer for small nozzle-to-plate spacings, when screens were placed in their slot nozzles immediately upstream of the nozzle exit plane. At larger spacings the effect of the screens was much smaller. This behavior was attributed to the effect of increased turbulence due to the screens, which caused the enhanced heat transfer for the small nozzle-to-plate spacings. However, as the spacing was increased, the high levels of turbulence generated by the jet mixing began to dominate and the turbulence characteristics affecting the heat transfer became independent of the characteristics induced just upstream of the nozzle exit plane. Apparently, for the present tests, even the presence of the wires attached to the plenum side of the jet plate midway between adjacent streamwise jet hole rows increased the turbulence levels enough to cause the observed 15% enhancement in heat transfer coefficients for z/d = 1, but this effect was suppressed at z/d = 2 and 3 due to turbulence generated by jet mixing.

5. CORRELATION

Correlation attempts were carried out primarily in terms of the variables indicated in Eq. (4.1). Consideration of the number of these variables (six in all, excluding Prandtl number) coupled with close examination of the data indicated the improbability of achieving a really tight correlation of simple form.

As alluded to earlier, least squares fits of the form $Nu = A\ Re_j^m$ to data sets for individual sizes at fixed values of the other parameters (G_c/G_j, x_n/d, y_n/d, and z/d) were excellent, though there was an apparently complex but not extremely sensitive variation of m with these parameters.

The plots in Fig. 4.2, previously examined, indicate that a crossflow functional form representing the dependence on G_c/G_j must, in general, be sensitive to x_n/d, y_n/d, and z/d; and that the sensitivity to z/d varies with x_n/d and y_n/d. For precise representation such a crossflow functional form would have to be monotonic decreasing for most values of x_n/d, y_n/d, and z/d, but for some cases with $z/d = 1$ would have to allow a broad, shallow minimum. Also, as previously discussed, Fig. 4.3 shows that for a given value of $G_c/G_j > 0$, Nu/Nu_1 increases monotonically with x_n/d, for $z/d = 1$, but is not monotonic with x_n/d for $z/d = 2$ and 3. In general, the form and sensitivity of the dependence of both Nu_1 (Fig. 4.1) and Nu/Nu_1 (Figs. 4.2 and 4.3) on any one of the independent variables can change depending on the values of the remaining independent variables for which it is examined. Also note that Fig. 4.4 indicates a different specific correlation is required for the staggered hole pattern, though the same functional form as for the inline pattern may be satisfactory.

A functional form which would properly incorporate in detail all the above features, even if it could be determined, would undoubtedly be extremely cumbersome and complex. After a number of attempts utilizing forms of varying types and complexity, the following form was finally adopted:

$$Nu = A\ Re_j^m\ \{1 - B[(z/d)(G_c/G_j)]^n\}Pr^{1/3} \qquad (5.1a)$$

where the coefficients A and B, and the exponents m and n are each permitted to depend on the geometric parameters in the form of simple power functions.

That is,

$$A,\ m,\ B,\ \text{and}\ n = C(x_n/d)^{n_x}(y_n/d)^{n_y}(z/d)^{n_z}. \qquad (5.1b)$$

The form (5.1) was applied separately to the inline and staggered hole pattern data for B, C, and D sizes. The analyses were carried out using a multivariable nonlinear regression routine with a least squares objective function [16]. The objective function was based on the logarithm of the dependent variable (Nu). In this way, the relative deviations rather than the absolute magnitudes were minimized. The resulting best fit values for the coefficients and exponents are summarized in Table 5.1 for both inline and staggered hole patterns.

Table 5.1 Constants for Use in Correlation Equation (5.1)

	Inline Pattern				Staggered Pattern			
	C	n_x	n_y	n_z	C	n_x	n_y	n_z
A	1.18	-0.944	-0.642	0.169	1.87	-0.771	-0.999	-0.257
m	0.612	0.059	0.032	-0.022	0.571	0.028	0.092	0.039
B	0.437	-0.095	-0.219	0.275	1.03	-0.243	-0.307	0.059
n	0.092	-0.005	0.599	1.04	0.442	0.098	-0.003	0.304

The inline correlation, based on a total of 1400 data points, produced a standard error of the deviations of 5.6%. By actual count 95% of the points fall within 11% of the fit line, while 99% fall within 16%. All the points fall within 19%, save one which deviated by 26%. The staggered correlation, based on a total of 680 points, produced a standard error of 6.1%. Ninety-five percent of these points were within 12% of the fit line, 99% were within 16%, and all the points fell within 18%, save one which again deviated by 26%. The bulk of the points having the larger deviations tended to occur for upstream rows for small Re_j at z/d = 1.

In an earlier report [2], the degree of consistency of the results obtained for geometrically similar configurations was assessed in detail. Least squares fits in the form $Nu = A\ Re_j^m$ were carried out for the combined data of the several sizes for each set of geometrically similar configurations. In effect, A and m were permitted to be adjustable constants taking different best fit values for each parameter set ($x_n/d, y_n/d, z/d$) and each spanwise row number (i.e., each value of G_c/G_j). Ninety-five percent of the points were within 7% of the respective fit lines, 99% were within 10%, and all were within 14%. These percentages give some indication of the best that might be done if the optimum functional form were to be found. Viewed in this context the proposed correlations appear to be quite acceptable.

Correlation lines calculated from Eq. (5.1) using values of the constants summarized in Table 5.1 are compared individually with the data for each inline geometry in Fig. 5.1 for $z/d = 1$, Fig. 5.2 for $z/d = 2$, and Fig. 5.3 for $z/d = 3$. In each individual graph of these Figures the shaded area represents the envelope of all data points for that geometry. The legend in each graph indicates the geometric sizes included, the geometric parameter values, the overall jet Reynolds number range, and the total number of points. The ordinate is the Nusselt number resolved to one streamwise hole spacing normalized by the value for the first upstream row Nu_1, at which $G_c/G_j = 0$. It should be emphasized that in preparing these plots the experimental values for Nu were normalized by the corresponding values of Nu_1 as calculated from the correlation equation. With corresponding correlated and experimental values of Nu normalized by the same value of Nu_1, a true comparison between the correlation and the data is maintained. It may also be emphasized that while the correlation is compared individually for each geometry in Figs. 5.1 through 5.3, the correlation itself is based on the data for all geometries. Obviously, improved correlations would result if limited to a single geometry. Overall the correlation appears to do an excellent job for $z/d = 2$ and 3 (Figs. 5.2 and 5.3), and an adequate job for $z/d = 1$ (Fig. 5.1).

The data for the A-size geometries listed in Table 2.1 were excluded from the data sets relied on for correlation for two reasons. First, the maximum heat transfer coefficient resolution for these data was two rather than one streamwise hole spacings. Second, as previously pointed out [2,4],

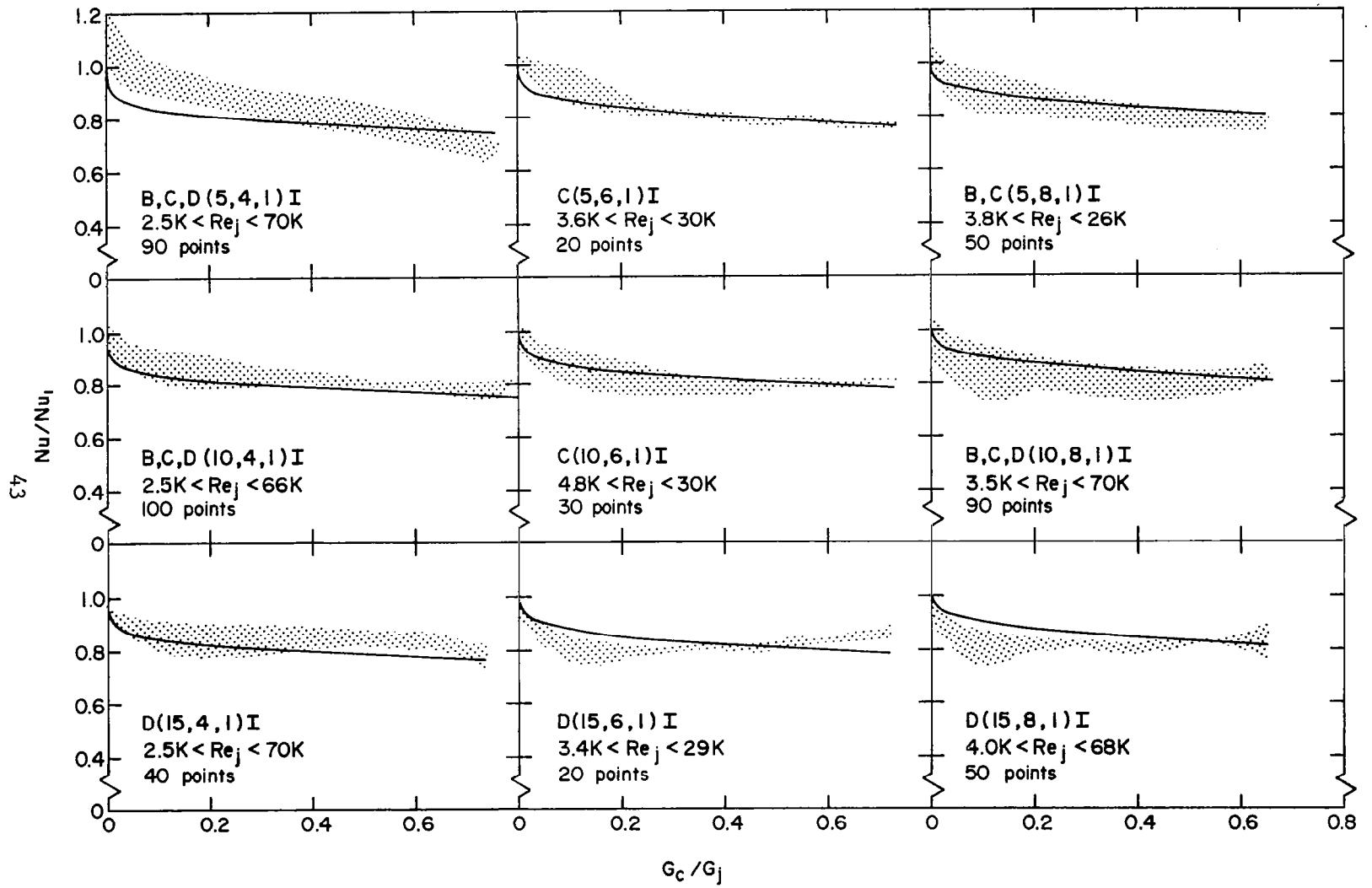

Fig. 5.1 Heat transfer correlation Eq. (5.1) compared with data for individual inline jet plate geometries, z/d = 1.

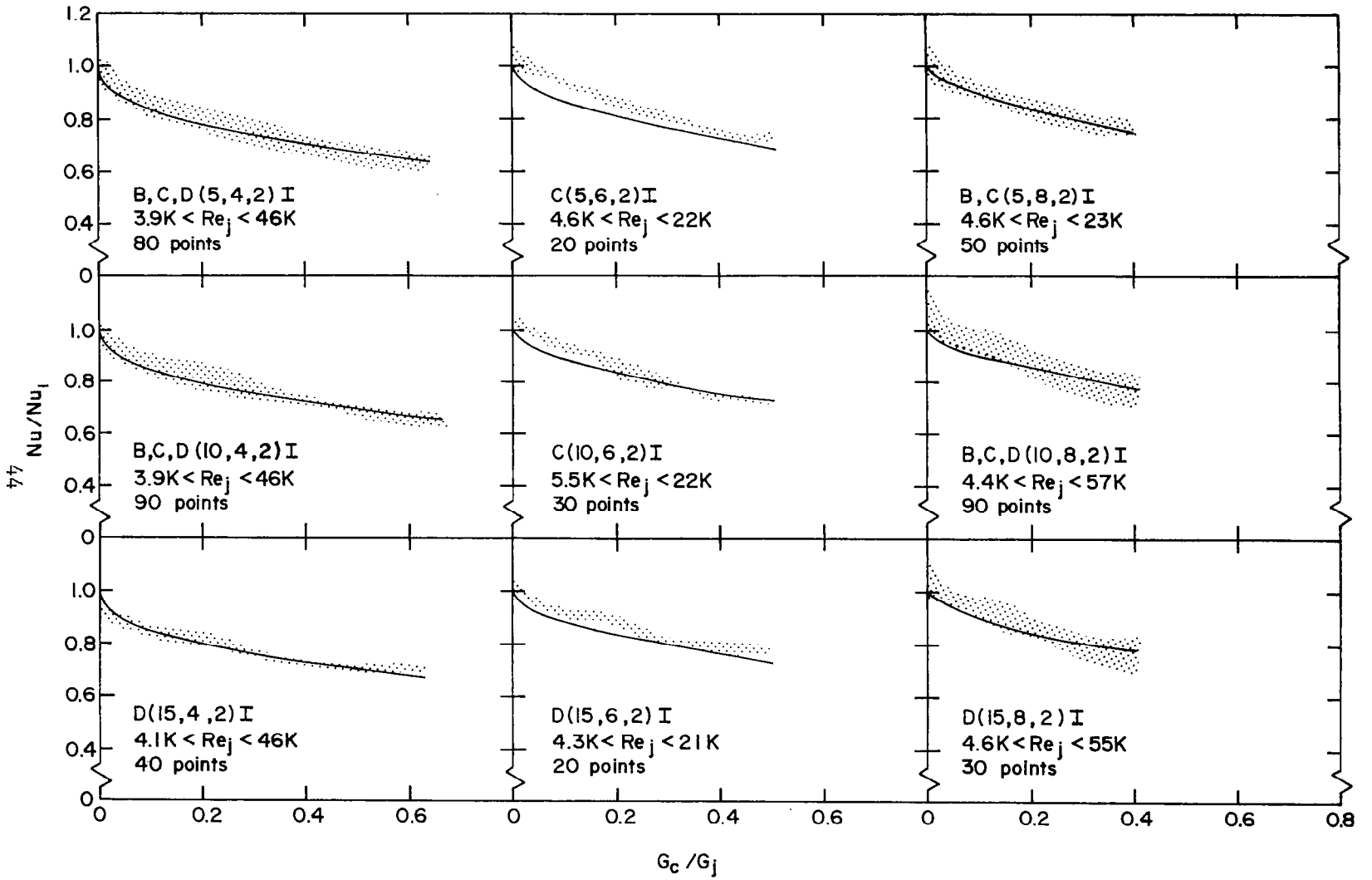

Fig. 5.2 Heat transfer correlation Eq. (5.1) compared with data for individual inline jet plate geometries, z/d = 2.

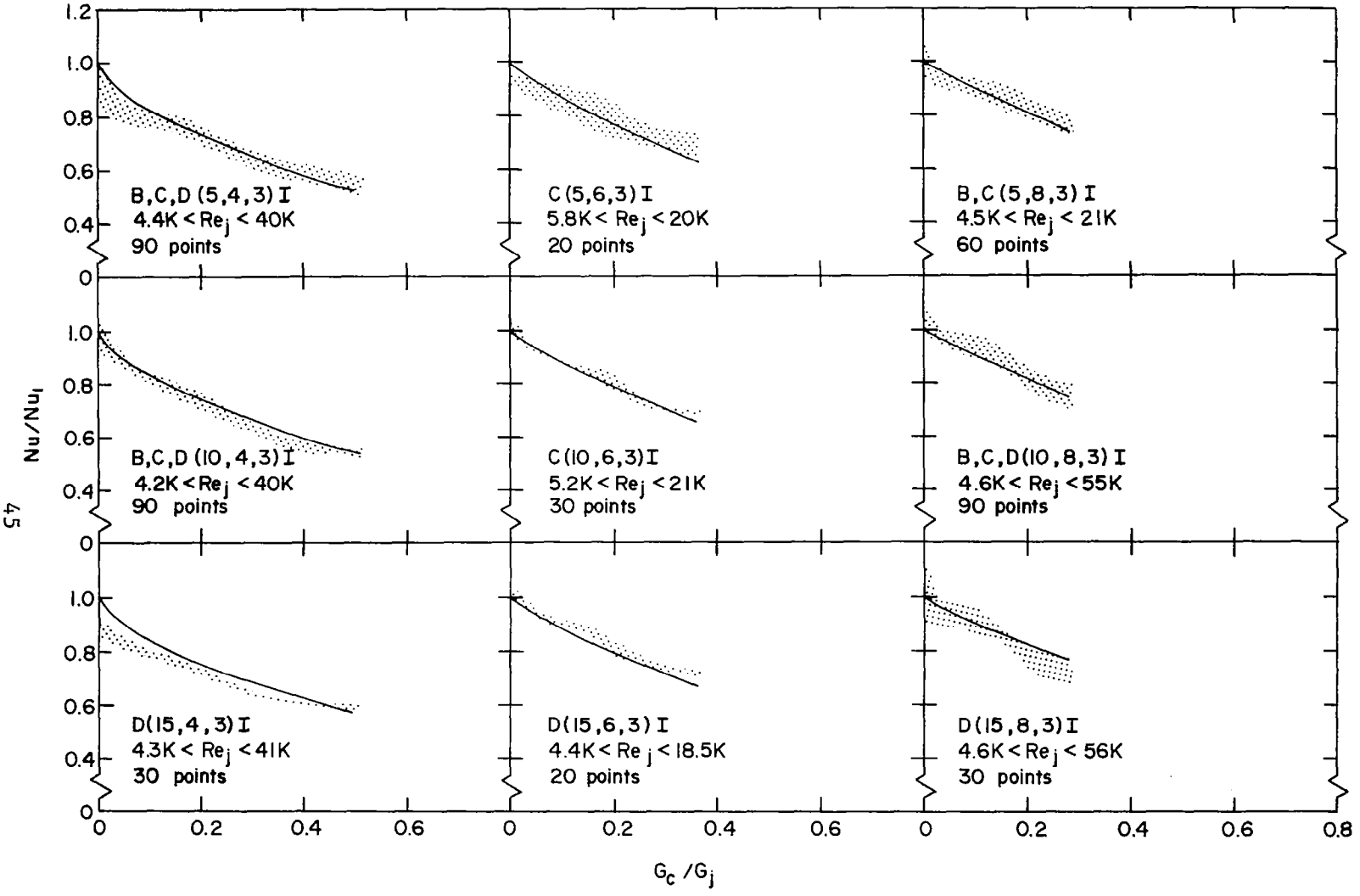

Fig. 5.3 Heat transfer correlation Eq. (5.1) compared with data for individual inline jet plate geometries, z/d = 3.

compressibility effects were present for these cases at the higher Reynolds numbers. This was due to the relatively low laboratory temperature and pressure levels at which the tests were run, combined with the small hole sizes and channel heights for A-size, resulting in pressure drops which were quite large relative to the pressure levels. This leads in some cases to choked flow conditions (see, e.g., Fig. 3.3).

The pressure and temperature levels in the anticipated turbine application are much higher with correspondingly lower Mach numbers. Therefore, considering the full range of Reynolds numbers, it is expected that the present data for sizes larger than A-size best model the prototype heat transfer characteristics for the gas turbine engine application. Many applications which, in fact, operate at low pressures utilize larger hole sizes and channel heights than for the present A-size. Thus, neither are compressibility effects present to a significant degree in these applications.

It is of interest, nevertheless, to compare the A-size data with the correlation. This was done for Nu resolved to $2x_n$. Despite the Mach numbers for some of these cases approaching or equal to unity, 95% of the points still fall within 16% of the correlation, with only one of 140 points deviating by more than 20% to a value of 27%. (The data used for the A(10,8,1)I case are a revised set recently obtained, which is more consistent with the corresponding B, C, and D size data than the original set documented in [2] and reported in [4]. This is the data obtained with no wire roughness elements present on the plenum side of the A(10,8)I jet plate, which was presented and discussed in Section 4.4.)

In developing the correlations, 50 data points for the highest flow rates for several B-size configurations ($\overline{Re}_j$ from 2.6 to 5.3×10^4) were also omitted because choked or nearly choked flow occurred (see, e.g., Fig. 3.1). However, when compared with the correlation 95% of these points are within 15%, the largest deviation being 18%.

Prior heat transfer measurements involving two-dimensional arrays of circular orifices in which the orifice plate and the heat transfer surface form a channel of uniform height with flow constrained to exit in a single direction parallel to jet hole rows were reported by Friedman and Mueller [5], Huang [6], Kercher and Tabakoff [7], and Chance [8]. These studies reported

mean heat transfer coefficients for the entire surface opposite the array [5], or values for spatial resolutions greater than or equal to one streamwise hole spacing [6,7,8]. Only Kercher and Tabakoff, and Chance measured streamwise flow distributions and suggested correlations for streamwise resolved heat transfer coefficients in terms of individual spanwise row jet and crossflow velocities. Kercher and Tabakoff's study included measurements for 16 different combinations of hole spacing and channel height. Only two of these combinations provided streamwise resolutions down to one streamwise hole spacing, and these had just four rows of holes. All were inline arrays with an aspect ratio (x_n/y_n) of unity. Their correlation requires use of three graphical presentations. Chance tested square, equilateral triangular, and rectangular arrays, but did not report specific hole spacings or numbers of holes for his jet plates, nor does his correlation include any distinction based on hole pattern.

Values of Nu_1 based on the present correlation are compared with those based on the Kercher and Tabakoff correlation in Fig. 5.4. The comparison is for square, inline arrays at the extreme values of the geometric parameters which fall within the ranges covered by both investigations. Results based on the correlation of Chance are also shown for cooling of the surface by the jets, which is the same condition under which Kercher and Tabakoff's and the present data were obtained. Chance's correlation for data with heating of the surface falls 10% above that shown in the Figure. The effect of crossflow as calculated from these same correlations is compared in Fig. 5.5 for the same geometries as Fig. 5.4.

Permitting both the coefficients and exponents in Eq. (5.1a) to depend on the geometric parameters provided the flexibility to achieve a reasonably tight overall correlation. This correlation is recommended for detailed analysis and design calculations, particularly when incorporated in computer programs where the larger number of specified constants is not a disadvantage.

An alternate correlation, more convenient for hand computation or examination of trends, is presented below. This correlation is of the same form as (5.1a), but with exponents m and n not permitted to depend on geometric parameters:

$$Nu/Nu_1 = 1 - C(x_n/d)^{n_x}(y_n/d)^{n_y}(z/d)^{n_z}(G_c/G_j)^n \qquad (5.2a)$$

where

$$Nu_1 = 0.363(x_n/d)^{-0.554}(y_n/d)^{-0.422}(z/d)^{0.068}Re_j^{0.727}Pr^{1/3} \qquad (5.2b)$$

and the constants in (5.2a) take the following values:

	C	n_x	n_y	n_z	n
Inline	0.596	-0.103	-0.380	0.803	0.561
Staggered	1.07	-0.198	-0.406	0.788	0.660

This correlation is essentially as good as that of Eq. (5.1) in terms of standard error and 95% confidence levels, but is not as tight overall.

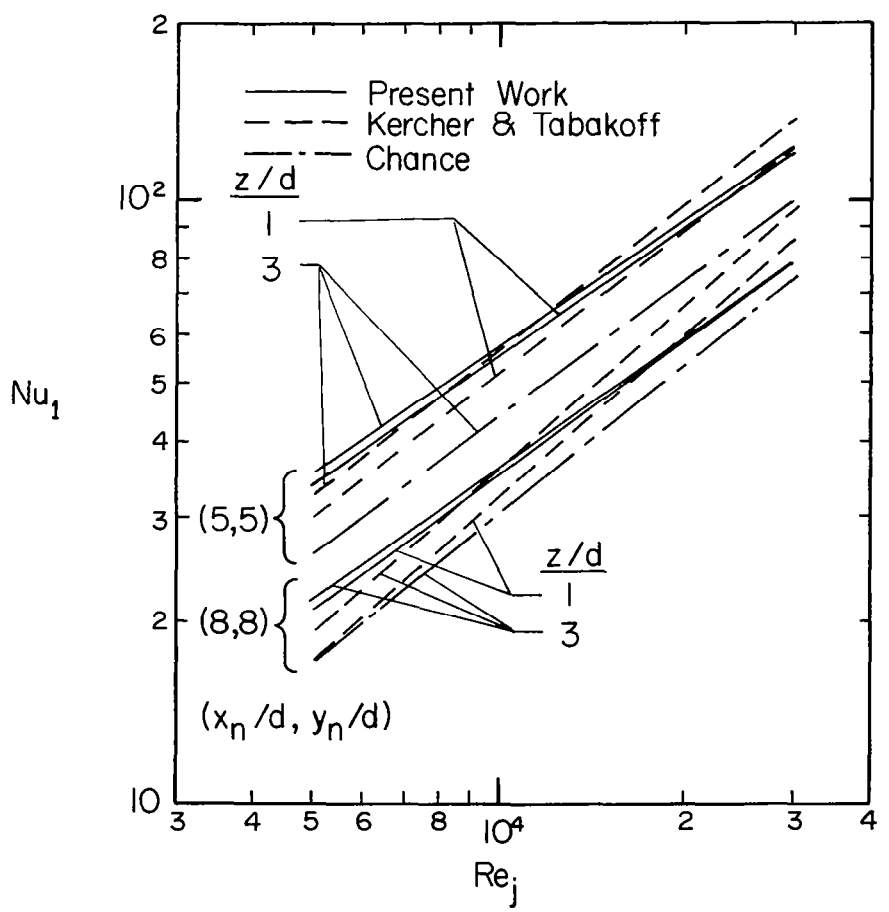

Fig. 5.4 Nusselt number for initial upstream row of array--Correlations compared.

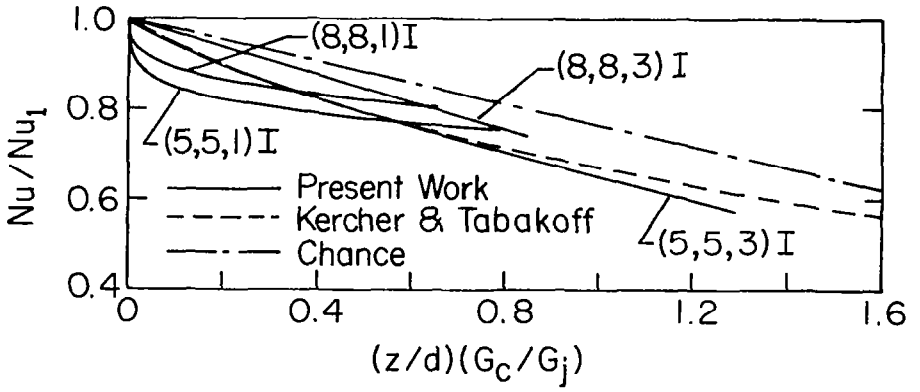

Fig. 5.5 Effect of crossflow on streamwise resolved Nusselt numbers--Correlations compared.

6. CONCLUSIONS

Experimentally determined heat transfer characteristics have been presented for jets of air issuing from arrays of circular orifices and impinging on a surface parallel to the jet orifice plate. Following impingement the air is constrained to exit in a single direction along the channel formed by the orifice plate and the impingement surface. Outlet flow from upstream jets imposes a crossflow on those downstream. The configurations tested model those of interest in current and contemplated designs for cooling of the midchord region of gas turbiine airfoils. Uniform rectangular hole patterns of both inline and staggered arrangements were included in the test program. Streamwise resolved, spanwise averaged heat transfer coefficients were measured for an isothermal impingement surface. Discharge coefficients for the jet orifice plates, as well as streamwise variations of the jet and channel crossflow velocities for the various configurations were also experimentally determined.

Streamwise hole spacings ranged from 5 to 15 jet hole diameters for inline patterns and 5 to 10 diameters for staggered patterns, spanwise spacings were 4 to 8 diameters, and channel heights (jet plate-to-impingement surface spacings) were 1 to 3 diameters. Hole pattern aspect ratios (ratio of streamwise-to-spanwise hole spacing) ranged from 0.625 to 3.75. The number of spanwise rows of jet holes was fixed at 10 for all configurations. Mean jet Reynolds numbers ranged from about $5x10^3$ to $5x10^4$. Overall, individual spanwise row jet Reynolds numbers were as low as $2.5x10^3$ and as high as $7x10^4$. The ratio of the channel crossflow velocity to the jet velocity ranged from zero (at the first upstream row) to as high as 0.8 downstream.

Conclusions reached are as follows:

(1) A simple one-dimensional, incompressible, momentum-flux model was found to satisfactorily predict the experimentally determined streamwise distributions of jet and channel crossflow velocities.

(2) Impingement surface heat transfer coefficients resolved in the streamwise direction to one streamwise hole spacing, averaged across the span, were satisfactorily correlated with the associated individual spanwise row jet and crossflow velocities, and with the geometric parameters. Separate correlations were required for the inline and staggered hole patterns, since the staggered patterns resulted in smaller heat transfer coefficients than their inline counterparts as hole spacings were decreased and channel height was increased. The correlations are, however, of the same form. Overall, 95% of the total of 2080 data points on which the correlations are based fall within 11% of the corresponding values predicted by the correlations.

(3) Jet plate discharge coefficients were found to be relatively insensitive to jet Reynolds number over the ranges covered. Mean values for individual jet plates ranged from 0.73 to 0.85. The mean value considering all jet plates was 0.79.

(4) Streamwise jet flow distributions ranged from highly nonuniform for a spanwise hole spacing of four hole diameters and a channel height of one diameter to essentially uniform for a spanwise spacing of eight diameters and a channel height of three diameters. The distributions were essentially independent of streamwise hole spacing and hole pattern (inline vs. staggered).

(5) Nusselt numbers varied with jet Reynolds numbers raised to a nominal power of 0.73.

(6) For a fixed jet Reynolds number and geometry the effect of increasing crossflow was to monotonically decrease the heat transfer coefficients, except for geometries having both larger hole spacings and channel heights of one hole diameter. In these latter cases decreases in heat transfer coefficients were followed by small increases, exhibiting a broad minimum over an intermediate range of crossflow-to-jet velocity ratios.

(7) Reduced values of heat transfer coefficients for staggered hole patterns relative to their inline counterparts are due to differences in the spanwise distribution of the crossflow. The crossflow for inline patterns tends to be channelized between adjacent streamwise jet rows, whereas for staggered patterns the crossflow is more nearly uniform across the channel span.

(8) The impingement surface heat transfer coefficients were independent of the thermal boundary condition existing at the surface of the jet plate which coincides with the orifice exit plane (the channel wall opposite the impingement surface).

(9) Roughness elements (wires) attached to the plenum side of one of the jet plates, midway between streamwise jet hole rows, increased the heat transfer coefficients by about 15% for the narrowest channel height of one hole diameter. The wires were originally installed for use as heating elements to control the jet plate surface thermal boundary condition resulting in conclusion (8) above.

(10) Caution should be exercised in applying the flow distribution model and the heat transfer correlations beyond the parameter ranges for which they have been verified.

(11) At the relatively low laboratory pressure levels at which the tests were conducted choked or nearly choked flow across the jet orifices occurred in several cases with small hole diameters at large flow rates. This heat transfer data was excluded from that on which the correlations are based. Nevertheless, 95% of these data points fall within 15% of the correlation.

REFERENCES

1. Gauntner, J.W., Gladden, H.J., Gauntner, D.J., and Yeh, F.C., ''Crossflow Effects on Impingement Cooling of a Turbine Vane,'' NASA TM X-3029, March 1974.

2. Florschuetz, L.W., Metzger, D.E., Takeuchi, D.I., and Berry, R.A., Multiple Jet Impingement Heat Transfer Characteristic -- Experimental Investigation of Inline and Staggered Arrays with Crossflow, NASA Contractor Report 3217, Arizona State University, Tempe, January 1980.

3. Florschuetz, L.W., Berry R.A., and Metzger, D.E., ''Periodic Streamwise Variations of Heat Transfer Coefficients for Inline and Staggered Arrays of Circular Jets with Crossflow of Spent Air,'' ASME Journal of Heat Transfer, Vol. 102, 1980, pp. 132-137.

4. Metzger, D.E., Florschuetz, L.W., Takeuchi, D.I., Behee, R.D., and Berry, R.A., ''Heat Transfer Characteristics for Inline and Staggered Arrays of Circular Jets with Crossflow of Spent Air,'' ASME Journal of Heat Transfer, Vol. 101, 1979, pp. 526-531.

5. Friedman, S.J., and Mueller, A.C., ''Heat Transfer to Flat Surfaces,'' Proceedings, General Discussion on Heat Transfer, The Institute of Mechanical Engineers, London, England, 1951, pp. 138-142.

6. Huang, G.C., ''Investigations of Heat Transfer Coefficients for Air Flow Through Round Jets Impinging Normal to a Heat Transfer Surface,'' ASME Journal of Heat Transfer, Vol. 85, 1963, pp. 237-243.

7. Kercher, D.M., and Tabakoff, W., ''Heat Transfer by a Square Array of Round Air Jets Impinging Perpendicular to a Flat Surface Including the Effect of Spent Air,'' ASME Journal of Engineering for Power, Vol. 92, 1970, pp. 73-82.

8. Chance, J.L., ''Experimental Investigation of Air Impingement Heat Transfer Under an Array of Round Jets,'' Tappi, Vol. 57, No. 6, 1974, pp. 108-112.

9. Gardon, R., and Cobonpue, J., ''Heat Transfer Between a Flat Plate and Jets of Air Impinging on It,'' International Developments in Heat Transfer, Proceedings of 2nd International Heat Transfer Conference, ASME, New York, 1962, pp. 454-460.

10. Hollworth, B.R., and Berry, R.D., ''Heat Transfer from Arrays of Impinging Jets with Large Jet-to-Jet Spacing,'' ASME Journal of Heat Transfer, Vol. 100, 1978, pp. 352-357.

11. Martin, H., ''Heat and Mass Transfer Between Impinging Gas Jets and Solid Surfaces,'' Advances in Heat Transfer, Vol. 13, Academic Press, New York, 1977, pp. 1-60.

12. Metzger, D.E., and Korstad, R.J., ''Effects of Cross Flow in Impingement Heat Transfer,'' ASME Journal of Engineering for Power, Vol. 94, 1972, pp. 35-41.

13. Bouchez, J.P., and Goldstein, R.J., ''Impingement Cooling from a Circular Jet in a Crossflow,'' International Journal of Heat and Mass Transfer, Vol. 18, 1975, pp. 719-730.

14. Sparrow, E.M., Goldstein, R.J., and Rouf, M.A., ''Effect of Nozzle-Surface Separation Distance on Impingement Heat Transfer for a Jet in a Crossflow,'' ASME Journal of Heat Transfer, Vol. 97, 1975, pp. 528-533.

15. Stoy, R.I., and Ben-Haim, Y., ''Turbulent Jets in a Confined Crossflow,'' ASME Journal of Fluids Engineering, Vol. 95, 1973, pp. 551-556.

16. Kuester, J.L., and Mize, J.H., Optimization Techniques with Fortran, McGraw-Hill, New York, 1973, pp. 240-250.

17. Gardon, R., and Akfirat, J.C., ''The Role of Turbulence in Determining the Heat Transfer Characteristics of Impinging Jets,'' International Journal of Heat and Mass Transfer, Vol. 8, 1965, pp. 1261-1272.